DEVELOPMENT OF ELECTRICALLY CONDUCTIVE POROUS SILK FIBROIN/CARBON NANOFIBER SCAFFOLDS

A THESIS SUBMITTED TO
THE GRADUATE SCHOOL OF NATURAL AND APPLIED SCIENCES
OF
MIDDLE EAST TECHNICAL UNIVERSITY

BY

YİĞİTHAN TUFAN

IN PARTIAL FULFILLMENT OF THE REQUIREMENTS
FOR
THE DEGREE OF MASTER OF SCIENCE
IN
METALLURGICAL AND MATERIALS ENGINEERING

AUGUST 2020

Approval of the thesis:

DEVELOPMENT OF ELECTRICALLY CONDUCTIVE POROUS SILK FIBROIN/CARBON NANOFIBER SCAFFOLDS

submitted by **YİĞİTHAN TUFAN** in partial fulfillment of the requirements for the degree of **Master of Science** i**n Metallurgical and Materials Engineering, Middle East Technical University** by,

Prof. Dr. Halil Kalıpçılar
Dean, Graduate School of **Natural and Applied Sciences** _____

Prof. Dr. Cemil Hakan Gür
Head of the Department, **Metallurgical and Materials Eng.** _____

Assoc. Prof. Dr. Batur Ercan
Supervisor, **Metallurgical and Materials Eng., METU** _____

Examining Committee Members:

Prof. Dr. Cevdet Kaynak
Metallurgical and Materials Eng, METU _____

Assoc. Prof. Dr. Batur Ercan
Metallurgical and Materials Eng, METU _____

Prof. Dr. Dilek Keskin
Engineering Sciences, METU _____

Assoc. Prof. Dr. Erhan Bat
Chemical Engineering, METU _____

Prof. Dr. Fatih Büyükserin
Biomedical Engineering, TOBB ETÜ _____

Date: 11.08.2020

I hereby declare that all information in this document has been obtained and presented in accordance with academic rules and ethical conduct. I also declare that, as required by these rules and conduct, I have fully cited and referenced all material and results that are not original to this work.

Name, Last name : Yiğithan Tufan

Signature :

ABSTRACT

DEVELOPMENT OF ELECTRICALLY CONDUCTIVE POROUS SILK FIBROIN/CARBON NANOFIBER SCAFFOLDS

Tufan, Yiğithan
Master of Science, Metallurgical and Materials Engineering
Supervisor : Prof. Dr. Mert Sertkaya
Co-Supervisor: Assoc. Prof. Dr. Batur Ercan

August 2020, 70 pages

Tissue engineering applications typically require porous scaffolds which provide requisite surface area for cellular functions, while allowing nutrient, waste and oxygen transport with the surrounding tissues. Concurrently, scaffolds should ensure sufficient mechanical properties to provide mechanically stable frameworks under physiologically relevant stress levels. Furthermore, electrically conductive platforms are also desired for the regeneration of specific tissues, where electrical impulses are transmitted throughout the tissue for proper physiological functioning. Towards this goal, silk fibroin (SF) from *Bombyx mori* silkworms captured significant interest in tissue engineering applications due to its tuneable mechanical properties and ability to promote cellular functions. In this thesis, carbon nanofibers (CNFs) were incorporated into porous SF matrix as a secondary phase to provide electrical conductivity and enhance mechanical properties of SF. In the meantime, pore size and porosity of SF/CNF nanocomposite scaffolds were controlled during scaffold fabrication via the salt leaching process. For the developed scaffold fabrication protocol, CNFs were dispersed in SF owing to the hydrogen bond forming ability of

hexafluoro-2-propanol (HFIP), a fluoroalcohol-based solvent used for SF. Results showed that SF/CNF nanocomposite scaffolds having electrical conductivities and tangent modulus values as high as 0.04 S/cm and 260 ± 30 kPa, respectively, were fabricated. In the meantime, these SF/CNF nanocomposite scaffold had pore size of 376 ± 53 μm and porosity as high as 78%. Furthermore, ~34% increase in the wettability of SF was achieved upon the incorporation of 10% CNF in SF scaffolds, which contributed to the enhanced fibroblast spreading on SF/CNF nanocomposite scaffold surfaces.

Keywords: Silk fibroin, carbon nanofiber, nanocomposite, mechanical properties, electrical conductivity

ÖZ

ELEKTRİKSEL İLETKENLİĞE SAHİP İPEK/KARBON NANOFİBER YAPIDA GÖZENEKLİ NANOKOMPOZİT DOKU İSKELESİ ÜRETİMİ

Tufan, Yiğithan
Yüksek Lisans, Metalurji ve Malzeme Mühendisliği
Tez Yöneticisi: Doç. Dr. Batur Ercan

Ağustos 2020, 70 sayfa

Doku mühendisliği uygulamalarında çoğunlukla gözenekli yapıdaki doku iskeleleri tercih edilmektedir. Bunun başlıca sebepleri arasında gözenekli yapının hücresel fonksiyonlar için gerekli olan yüzey alanını sunması ve hücrelerin çevre doku ile besin, atık ve oksijen transferi yapmalarına imkan sağlaması yer almaktadır. Bununla birlikte, doku iskelelerinin mekanik özellikleri fizyolojik ortamdan kaynaklı yükleri taşıyabilecek yeterlilikte olmalıdır. Ayrıca, fizyolojik fonksiyonların yerine getirilebilmesi için doku boyunca elektriksel impalsların iletildiği dokularda elektriksel iletkenliğe sahip doku iskelelerine ihtiyaç duyulmaktadır. Bu doğrultuda, ayarlanabilir mekanik özellikleri ve hücre fonksiyonları üzerindeki olumlu etkileri nedeniyle Bombyx mori ipek böceklerinin kozalarından elde edilen ipek fibroin (SF), doku mühendisliği uygulamaları için önem kazanmıştır. Bu tez çalışmasında, gözenekli yapıdaki ipek fibroin doku iskelelerine elektriksel iletkenlik kazandırmak ve mekanik dayanımlarını artırmak amacıyla ikincil faz olarak karbon nanofiberler (CNF) eklenmiştir. Geliştirilen üretim metodunda, flor bazlı bir alkol olan hexafluoro-2-propanol (HFIP)'ün (SF çözücüsü olarak kullanılmaktadır) hidrojen bağı kurma yetisi kullanılarak CNF'ler SF içerisine dağıtılmıştır. Spesifik olarak, 0.04 S/cm'ye ulaşan elektriksel iletkenliğe ve 260 ± 30 kPa'ya ulaşan esneklik

katsayısına sahip SF/CNF nanokompozit doku iskelesi üretilmiştir. Bu doku iskelesi %78 porozitede olup, ortalama 376 ± 53 μm boyutunda gözeneklere sahiptir. Ayrıca, %10 CNF eklenmesi sonucunda SF'nin ıslanabilirliğinde ~%34'lük bir artış elde edilmiştir. Bu artışa bağlı olarak fibroblastların SF/CNF nanokompozit yüzeylerinde SF'ye kıyasla daha fazla yayılıma uğradıkları tespit edilmiştir.

Anahtar Kelimeler: İpek fibroin, karbon nanofiber, nanokompozit, mekanik özellikler, elektriksel iletkenlik

To my true love and my beloved parents

ACKNOWLEDGMENTS

I wish to express my deepest gratitude to my supervisor Assoc. Prof. Dr. Batur Ercan for his guidance, advice, criticism, encouragements and insight throughout my studies. Thanks to his enthusiasm and deep academic vision, I learned a lot from him starting my undergraduate education. As a matter of fact, I owe him everything I learned within this period. In addition to his guidance in my studies, he was always helpful in every respect and I am grateful for his personal generosity.

I would also like to thank Çağatay Mert Oral for his friendship. Special thanks to Assoc. Prof. Dr. Bora Garipcan for his suggestions and comments and Ms. Hayriye Öztatlı for her help in biological experiments. Also, the assistance of Ms. İpek Tuğçe Döş in scaffold fabrication is gratefully acknowledged.

I would like to thank BIOMATEN-METU Center of Excellence in Biomaterials and Tissue Engineering and METU Central Laboratory for their support in scaffold characterization. Special thanks to Dr. Senem Heper Büyüksungur, Dr. Ezgi Antmen, Dr. İbrahim Çam and Serkan Yılmaz for their help in the characterization studies. I am thankful to Dr. Arda Büyüksungur for his help in micro-CT analyses and scientific discussion.

This work was financially supported by The Scientific and Technological Research Council of Turkey (Grant no: 117M754). This work was partially supported by BAGEP Program of The Science Academy, Turkey, GEBIP program of Turkish Academy of Sciences, Turkey and Boğaziçi University Research Fund by Grant Number 6701.

TABLE OF CONTENTS

LIST OF TABLES

TABLES

LIST OF FIGURES

FIGURES

CHAPTER 1

INTRODUCTION

Tissue engineering is a developing field for the treatment of damaged tissues [1]. The field is structured on the use of scaffolds as temporary mechanical supports for the engraftment of cells to the injury site to induce tissue regeneration [2][3]. The use of scaffolds in tissue engineering is schematically illustrated in Figure 1.1. Briefly, cells are isolated from the patient, cultivated *in vitro* and seeded into porous scaffolds [4]. Then, the scaffolds are transplanted to the damaged region for the regeneration of healthy tissues. Depending on the origin and nature of isolated cells, they can be seeded directly into the scaffolds or differentiated prior to seeding during *in vitro* cell expansion. Scaffolds used in tissue engineering should provide an appropriate environment for cellular adhesion, as well as nutrient and oxygen transportation with the surrounding tissues [5]. Concurrently, they should allow cells to produce their own extracellular matrix and be gradually replaced with body's own cells owing to their biodegradation characteristics [6]. Additionally, scaffolds should have similar mechanical properties with the host tissue for proper physiological functioning [7].

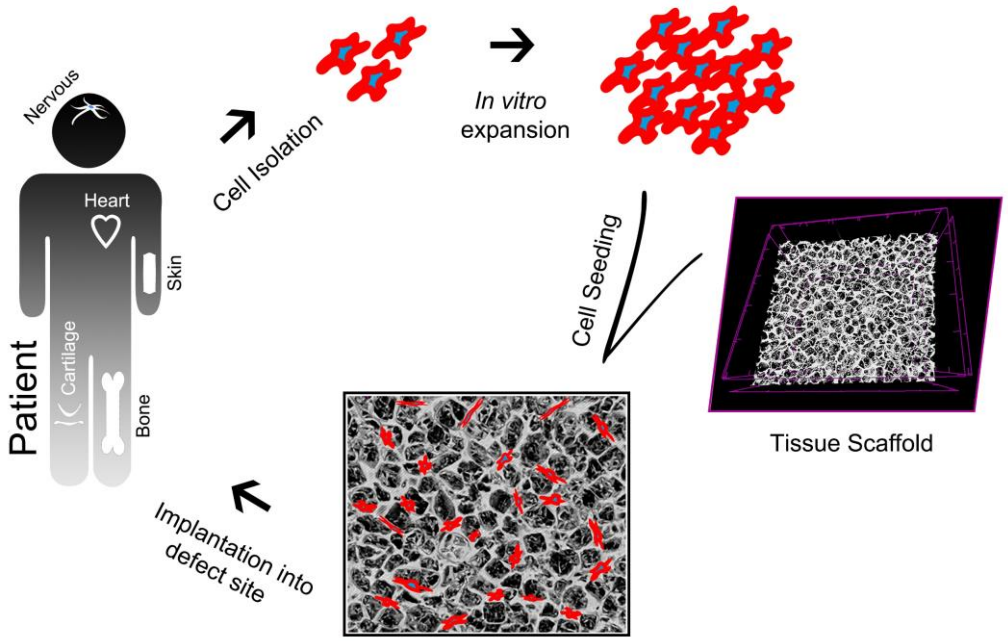

Figure 1.1. The use of scaffolds in tissue engineering applications.

Examples of tissues investigated for tissue engineering include, bone, cartilage, skin, neural, heart tissues and etc [6]. The choice of material and fabrication method should be precisely engineered to fulfil the requirements of the tissue and organ in question. For example, in bone tissue engineering, natural polymeric materials such as chitosan, collagen and silk have been combined with calcium phosphates to mimic the structure and properties of bone tissue (30% w/v organic collagen fibrils and 70% inorganic calcium phosphate crystals) [8]. On the other hand, for nerve regeneration, scaffolds were designed to mimic physical and mechanical properties of peripheral neural tissue [9]. Synthetic and natural polymeric materials, such as polylactic acid (PLA), poly(ε-caprolactone) PCL, collagen, silk and their composites, were utilized to obtain flexible and electrically conductive scaffolds for neural regeneration [9]. Similarly, scaffolds utilized for cardiac tissue engineering (CTE) should provide mechanical integrity, electrical conductivity, biodegradability and optimal biological interactions with the host tissue for enhanced cellular activity and vascularization [10]. Though several synthetic and natural polymeric materials, including ploy(lactic acid) [11], poly(glycolic acid) [12], chitosan [13] and alginate [14], as well as polymer-nanocomposites like PCL/carbon nanotube [15] and alginate/gold

nanowires [16] were explored for CTE, more research is required for their translation into clinics [10].

1.1 Silk Fibroin

Bombyx mori silkworm silk fibroin (SF), well-known for its strength and luster, has not only been used as a luxury textile fiber but also as a suture material for centuries [17]. In the last 2 decades, silk based biomaterials captured considerable attention of the scientific community owing to their unique properties, including high strength and toughness, biocompatibility, biodegradability and ability to fabricate in different material forms [18]. Also, large-scale production of silk for the textile industry made it an abundant material with a reasonable cost [17]. *Bombyx mori* silkworms (the main producer of silk worldwide) spin cocoon silk (Figure 1.2a and 1.2b) at their fifth instar stage and use it as a protective covering until growing to the moth stage [19]. Raw cocoon silk is a protein based material consisting of two parallel fibroin fibers encapsulated inside a sericin outer lining, which holds the fibroin fibers together as shown in Figure 1.2c [20]. Silk fibroin, the main structural component of the cocoon, is purified from sericin upon degumming the raw silk to be used in different material forms [21]. The unique properties of SF originated from its hierarchical structure (Figure 1.2d and 1.2e) starting from the molecular level (~3Å) up to final form (~15 μm).

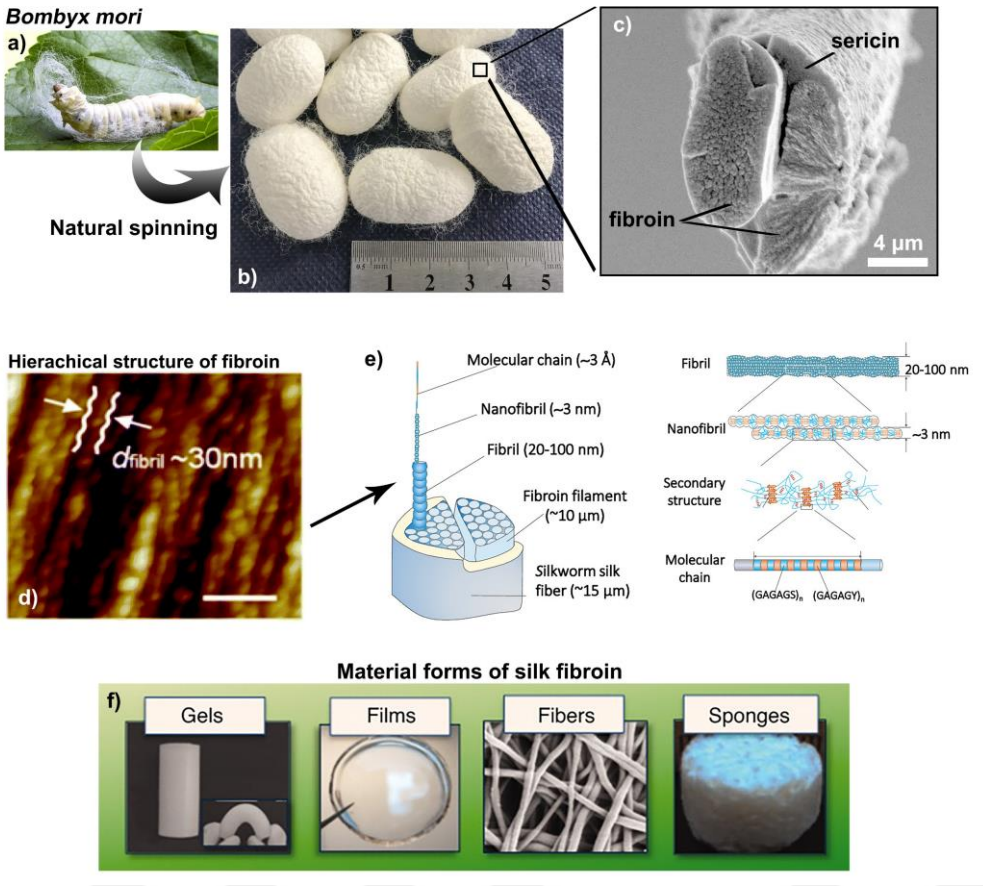

Figure 1.2. a) *Bombyx mori* silkworm, b) *Bombyx mori* silkworm silk cocoon, c) cross-sectional SEM image of raw silk showing sericin and fibroin [22], d) AFM image showing the fibroin fibrils [23], e) schematic drawing illustrating the hierarchical structure of silk fibroin [24] and f) various material forms of silk fibroin [25].

Examples of silk fibroin material forms include, but are not limited to, gels, films, fibers and sponges (Figure 1.2f) [25]. This variety in the final material form of SF is due to its ability to be solubilized in ionic solutions including lithium salts or $CaCl_2$/ethanol/water solutions [26]. Once these solutions are dialyzed, SF remains stable as an aqueous solution (for a limited time) for use in numerous fabrication methods [17]. Alternatively, for long term storage, SF solutions can be lyophilized after the dialysis step. In this case, another solvents, *i.e.* 1,1,1,3,3,3-hexafluoro-2-

propanol (HFIP) can be used to dissolve lyophilized SF; and then, the solution can be used in the fabrication of different material forms [17][26].

The ability of SF to be fabricated in different material forms offers a diversity in its physicochemical, mechanical, biological and degradation properties [27]. Also, the aforementioned properties could be fine-tuned through the optimization of SF fabrication parameters [27]. For example, mechanical properties for different material forms of SF vary considerably, as listed in Table 1.1 [20]. It is also clear in Table 1 that the mechanical properties of a SF material form can be tailored by altering its porosity, pore size and SF concentration.

Table 1.1 Mechanical properties of different SF material forms [20]

Material form (SF concentration)	Pore size (μm)/porosity (%)	Young's Modulus (GPa)	Ultimate Tensile Strength (Mpa)
Methanol treated sponges (6 wt%)	151±40 / 87.6	0.00043	0.02
HFIP-derived sponges (17 wt/v%)	15-202 / -	0.00045-0.001	0.175-0.25
Aqueous-derived sponges (4 wt/v%)	940±50 / 95	0.00007	0.011
	760±30 / 95	0.00008	0.011
	650±30 / 97	0.0001	0.012
	570±30 / 97	0.000115	0.013
	470±30 / 97	0.00013	0.013
Aqueous-derived sponges (8 wt/v%)	920±50 / 92	0.0013	0.1
	750±20 / 94	0.00153	0.125
	640±30 / 95	0.00194	0.14
Aqueous-derived sponges (10 wt/v%)	920±50 / 85	0.00333	0.32
Hydrogels (8 wt/v%)	-	-	0.0252
Films (as cast)	-	3.9	47.2
Films (methanol-treated)	-	3.5	58.8
Films (water-annealed)	-	1.9	67.7
Films (ultrathin, layer by layer assembly)	-	6-8	100
Electrospun mat (3 wt%)		-	15

1.2 Structure of Silk Fibroin

SF consists of heavy (350 kDa) and light (25 kDa) polypeptide chains which are linked together with a single disulphide bond [28]. The light chain of SF mainly contains of alanine (14%), serine (10%) and glycine (9%) amino acids, whereas the majority of SF heavy chain is composed of glycine (G) (45.9%), alanine (A) (30.3%), serine (S) (12.1%), tyrosine (Y) (5.3%) and valine (1.8%) residues (their molecular structures are given in Figure 1.3a [29]. SF heavy chain consists of large hydrophobic repetitive domains that are intervened by smaller hydrophilic non-repetitive domains, as illustrated in Figure 1.3b [20]. In detail, majority of the heavy chain contains GAGAGS and GAGAGY repeats, where they constitute 72% of the overall repeat units [30]. These repeating units play a critical role for the secondary structure of SF. For example, GAGAGS was reported to be the only unit that can form β-sheet crystallites, whereas GAAS tetrapeptides were responsible for the formation of β-turns [30]. Therefore, the hydrophobic amino acid sequence of the heavy chain, mainly the $(GAGAGS)_n$ repeats is capable of forming β-sheet crystallites via intermolecular forces and these highly ordered β-sheet crystallites embedded within an amorphous matrix are responsible for superior mechanical properties of SF [31][32].

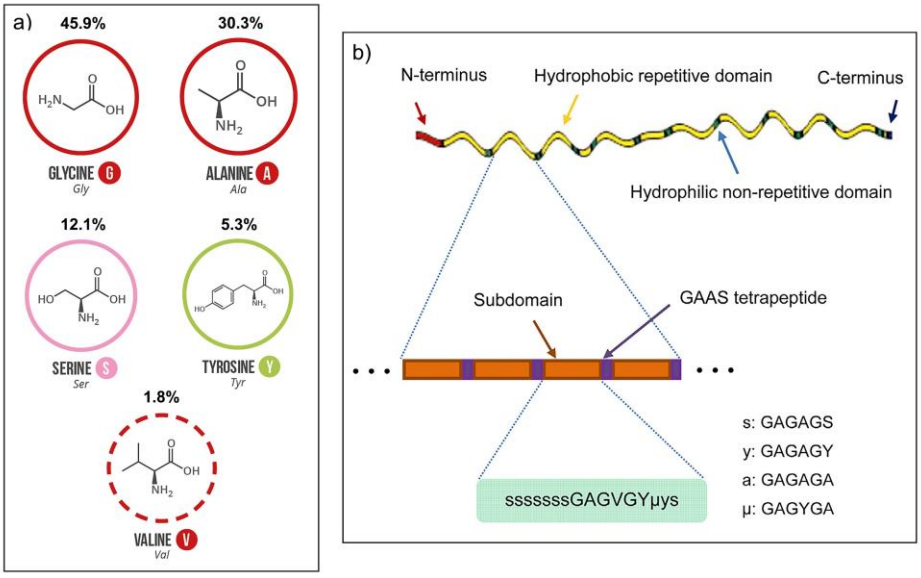

Figure 1.3. a) Chemical structures of the most abundant amino acids in SF and b) primary structure of SF [33].

Secondary structures of proteins refer to the folded polypeptides which are stabilized by hydrogen bonds between the amine and carboxyl groups of amino acids [30]. The most common secondary structures, α-helices and β-sheets, were illustrated in Figure 1.4a. There are also β-turns located at the regions where polypeptide chains change folding directions (Figure 1.4a). The unfolded polypeptide chains are generally referred as random coil [30]. Though an individual hydrogen bond is weaker than a covalent bond, large numbers of hydrogen bonds in α-helices and β-sheets highly reinforce the interactions between polypeptide chains and greatly enhance the strength of these secondary structures [30].

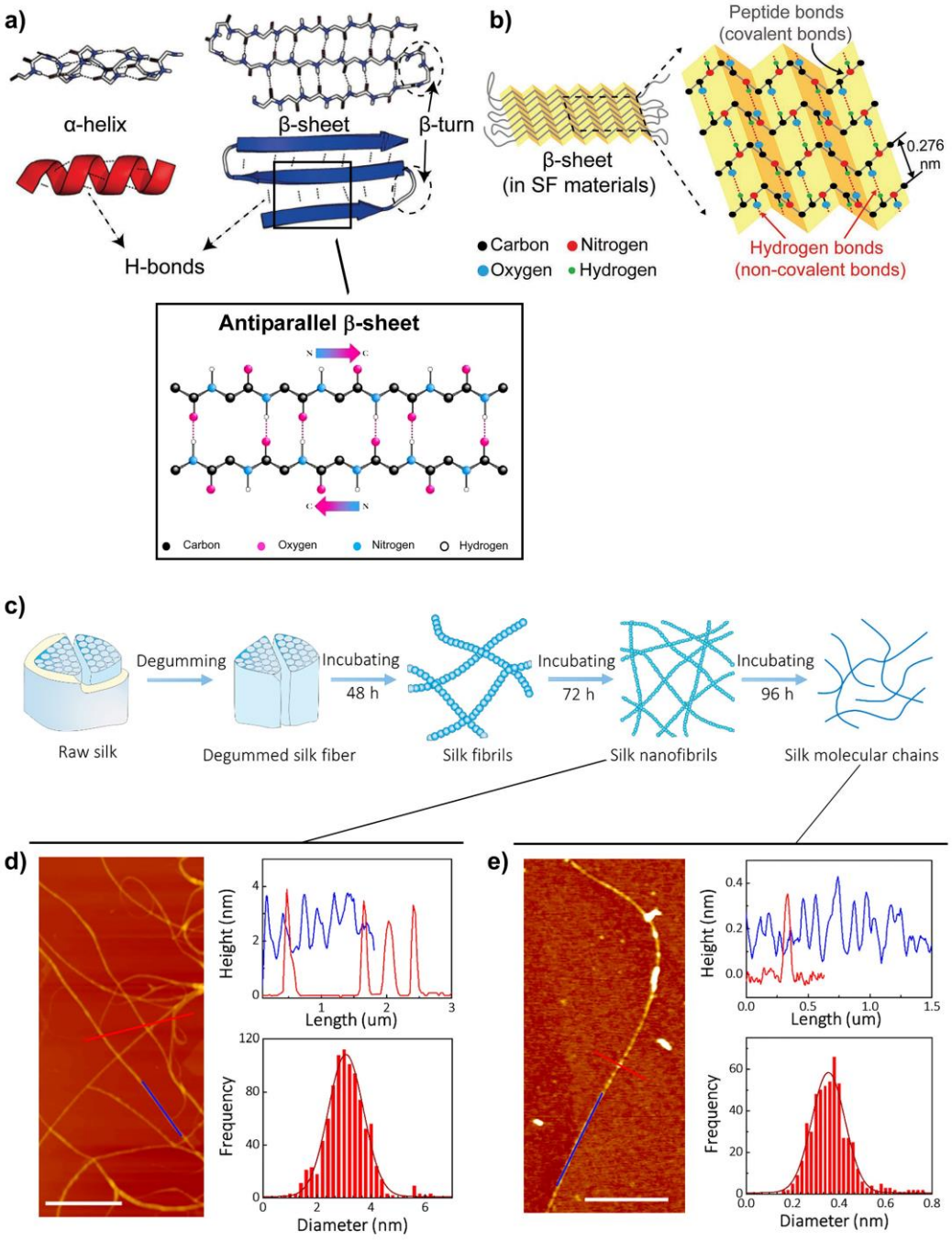

Figure 1.4. a) The most common secondary structures of SF [30], b) illustration of β-sheets in SF [30], c) hierarchical structure of SF [24] and AFM analyses of d) silk nanofibrils and e) silk molecular chains [24].

The remarkable strength of SF arose from β-sheet crystallites (the tertiary structure of SF) [34]. They are formed when several adjacent β-sheets (Figure 2b) from different molecules are stacked in a raw forming hydrogen bonds as well as hydrophobic and van der Waal's interactions between adjacent layers [30]. For convenience, β-sheets are considered as 2D crystals, whereas β-crystallites are crystals in 3D [30]. The latest study investigating the structure of SF exhibited its hierarchical structure (Figure 1.2e) composed of molecular chains, nanofibrils, fibrils and fibers, from the lowest dimension up to macro levels, respectively (Figure 1.4c) [24]. AFM analyses of two hierarchical levels, nanofibrils and molecular chains (Figure 1.4d and Figure 1.4e, respectively) of SF, revealed that SF nanofibrils have ~3 nm diameter whereas SF molecular chains has a diameter of 3.7 ± 0.9 Å.

1.3 SF Based Scaffold Design for Tissue Engineering Applications

SF based biomaterials were proposed for various tissue engineering applications, including bone, cartilage and skin regeneration, urethral and corneal reconstruction, as well as cardiac regeneration [35][36][37][38][39][40][41][42]. 3D porous architectures were generally preferred in these applications as they provided higher surface area for cell adhesion and proliferation, better cell/scaffold integration and nutrient/waste transportation [43]. One of the main advantages of using SF scaffolds in tissue engineering was the ability to control its 3D porous architecture through the alteration of fabrication parameters (mainly the total pore volume and mean pore size), which in turn governs mechanical properties and biological interactions [44]. However, sub-optimal mechanical properties of 3D scaffolds under physiologically relevant stresses was a major concern. As a matter of fact, the lack of an ideal porous architecture to satisfy both the mechanical and the cellular requirements impeded their widespread adaption in clinical settings for various tissue engineering applications. Therefore, 3D scaffolds require the ability to maintain their physical characteristics under biomechanical stresses, allow infiltration and proliferation of cells within their porous architecture and promote tissue regeneration.

Although there were several studies investigating the effect of porous architecture on scaffold properties, conflicting results exist on the optimal pore size range of scaffolds for tissue formation. For instance, SF scaffolds utilized for bone tissue engineering having a pore size range of 400-600 μm induced higher bone protein secretion and calcium deposition compared to scaffolds that have pore size ranges of 250-500 μm and 500-1000 μm [45]. On the other hand, when human bone marrow derived mesenchymal stem cells (hMSCs) were cultured on SF scaffolds, the ones having a pore size range of 112-224 μm exhibited the most efficient extra cellular matrix mineralization [46]. For cartilage regeneration, the mean pore size of ~500 μm was found to be the most beneficial for chondrogenic differentiation [47], whereas SF scaffolds having 71–210 μm pore size were observed to enhance adhesion, viability and proliferation of MSCs for cartilage regeneration [48]. Moreover, Di Felice *et al.* [49] suggested enhanced cardiac protein expression and extra cellular matrix synthesis of rat cardiac progenitor cells on SF scaffolds having pores in the size range of 200-400 μm. Nonetheless, it's worth noting that the origin and types of cells used in these studies might vary and lead to the conflicting results on the optimal pore size range of scaffolds.

Along with mean pore size, SF concentration was another important parameter in the design of SF scaffolds. In fact, studies showed altered cellular interactions and mechanical properties of SF scaffolds upon the changes in porosity and SF concentration. For instance, Mandal *et al.* [50] investigated human dermal fibroblast functions on *Antheraea mylitta* SF scaffolds and observed improved cellular migration and proliferation on scaffold having higher porosity. In a follow-up study [51], the effect of SF concentration on cellular adhesion and proliferation was investigated for SF films upon the changes in SF concentration. It was suggested that 2 w/v % SF films supported MSC proliferation better than SF films with 4 and 6 w/v % concentrations. On the other hand, Rnjak-Kovacina *et al.* [52] observed that there was no significant difference in hMSC proliferation on SF scaffolds having 0.5, 1, 2 and 4 w/v % SF concentrations. Interestingly, when bone marrow derived stromal

cells (BMSCs) were cultured on SF scaffolds, the viability of cells were shown to be significantly higher on 5 w/v % SF scaffold compared to 3, 7 and 9 w/v % SF scaffolds [53]. In addition, a gradual decrease in the pore size with an increasing SF concentration was reported where 5 w/v % scaffolds had the optimal pore size (~120 μm) for the proliferation of BMSCs [53].

In addition, elastic modulus of a scaffold was critical in regenerative therapies where a scaffold having an elastic modulus matching that of host tissue could better support biomechanical stresses, while inducing native-like tissue regeneration faster *in vitro* and *in vivo*. Since the mechanical properties of different tissues differ considerably, *i.e.* elastic modulus of cortical bone is 15-25 GPa [54], skin tissue is ~30 MPa [55] and heart muscle tissue is 50-100 kPa [56], the ability to SF scaffolds to be fine-tuned for desired mechanical properties provides a major advantage. Among the scaffold characteristics that govern mechanical properties, SF concentration, total pore volume, mean pores size and the uniformity of porous microstructure are particularly important [57]. For instance, compressive moduli of SF scaffolds were inversely proportional with mean pore size, where the modulus increased from 70 ± 5 kPa up to 130 ± 10 kPa upon a decrease in the mean pore size from 940 ± 50 μm to 470 ± 30 μm (porosities of these scaffolds were 95 ± 1.8 and 97 ± 0.5, respectively) [58]. In addition, the compressive moduli of scaffolds also increased with increasing SF concentration; for instance, 100 ± 5 kPa was reported for 4 w/v % SF scaffolds, whereas 1940 ± 240 kPa was reported for 8 w/v % SF scaffolds (no significant difference was reported between their pore sizes and porosities) [58]. Researchers correlated the increased elastic modulus upon the increase in SF concentration with cellular morphology. Specifically, increasing the SF concentration from 0.5 to 4 w/v % resulted in a modulus increase from 44.50 ± 18.08 to 321.33 ± 49.38 kPa, which was proposed to induce a more spread hMSC morphology. Furthermore, Engler *et al.* [59] observed that matrices having lower elastic modulus induced MSC differentiation into neuronal lineage, yet the ones having higher elastic modulus up-regulated osteogenic genes. Similarly, polyethylene glycol dimethacrylate hydrogels

having lower scaffold elasticity (3 kPa) was found to direct expression of endothelial markers in MSCs, whereas expression of smooth muscle cell markers was demonstrated on hydrogels with higher elasticity (>8 kPa) [60]. Therefore, the proper choice of scaffold material might provide an advantage to fine tune mechanical and biological properties through a well-designed 3D porous architecture.

1.4 Carbon Nanofiber Reinforced Silk Fibroin Composites for Tissue Engineering Applications

Electrically conductive platforms were shown to enhance tissue regeneration, especially for neural and heart muscle tissues, where electrical impulses had a significant role in physiological functioning [61][62]. As a matter of fact, electrically conductive tissue scaffolds having similar electrical conductivities to that of native tissue were needed for proper physiological functioning and faster tissue regeneration [63]. For instance, a cardiac patch should have a conductivity range of 5×10^{-3} to 0.16 S/cm to mimic cardiac tissue [64]. To achieve this, electrically conductive secondary phase reinforcements including graphene, carbon nanotubes (CNTs) and carbon nanofibers (CNFs) were proposed for tissue engineering scaffolds [65][66]. Among the conductive secondary phase additives, CNFs offer high aspect ratio, low toxicity, high dispersion in aqueous media and ability to be easily functionalized [66][67]. An individual carbon nanofiber can be considered as stacks of curved graphene sheets with a certain angle (nanocones) as shown in Figure 1.5a [68]. The high aspect ratio of CNFs (Figure 1.5b), *i. e.* the average diameter of ~100 nm with a length up to 200 μm, was beneficial to reach percolation threshold for electrical conductivity (Figure 1.5c) when used as a secondary phase reinforcement [69]. It was demonstrated in Figure 1.5d that poor dispersion inhibits the network formation, whereas good dispersion (whether the formation of CNF bundling or not) together with good distribution (the way the CNFs fill the space) might still lead to gaps between CNFs to prevent electrical conductivity [69].

Therefore, good dispersion of CNFs while remaining their physical contact was essential to obtain electrical conductivity inside an insulating matrix [69].

There were several studies revealing the potential of CNFs for use in biomedical applications [70][71][72]. For instance, enhanced metabolic activity of neonatal rat cardiomyocytes and increased expression of cardiac specific genes were observed on electrically conductive chitosan/CNF scaffolds compared to non-conductive ones [73]. It was also demonstrated that electrically conductive scaffolds promoted enhanced myotube maturation compared to their non-conductive counterparts in skeletal muscle tissue [74]. Webster *et al.* [75] investigated the effect of CNF on neural and osteoblast cell functions using PU/CNF composite substrates. Their results suggested that PU/CNF composites supported neurite extensions and enhanced osteoblast functions. In another study where the interactions of neurons and cardiomyocytes with PLGA/CNF composites were investigated, electrically conductive composites having 75 wt. % CNF revealed increased cardiomyocyte density up to 5 days *in vitro* [76]. A similar trend was also obtained for neurons, *i.e.* neuronal density was significantly higher on CNF containing conductive PLGA composites after 4 days of culture [76]. SF/CNF composite films having various CNF concentrations revealed that nanocomposite films were cytocompatible up to 5:100 CNF:SF weight ratio [66]. In another study, growth factor loaded porous SF/CNF scaffolds were investigated for orthopedic applications [77]. The detailed *in vitro* and *in vivo* studies revealed that SF/CNF scaffolds promoted successful bone regeneration with minimal inflammatory response.

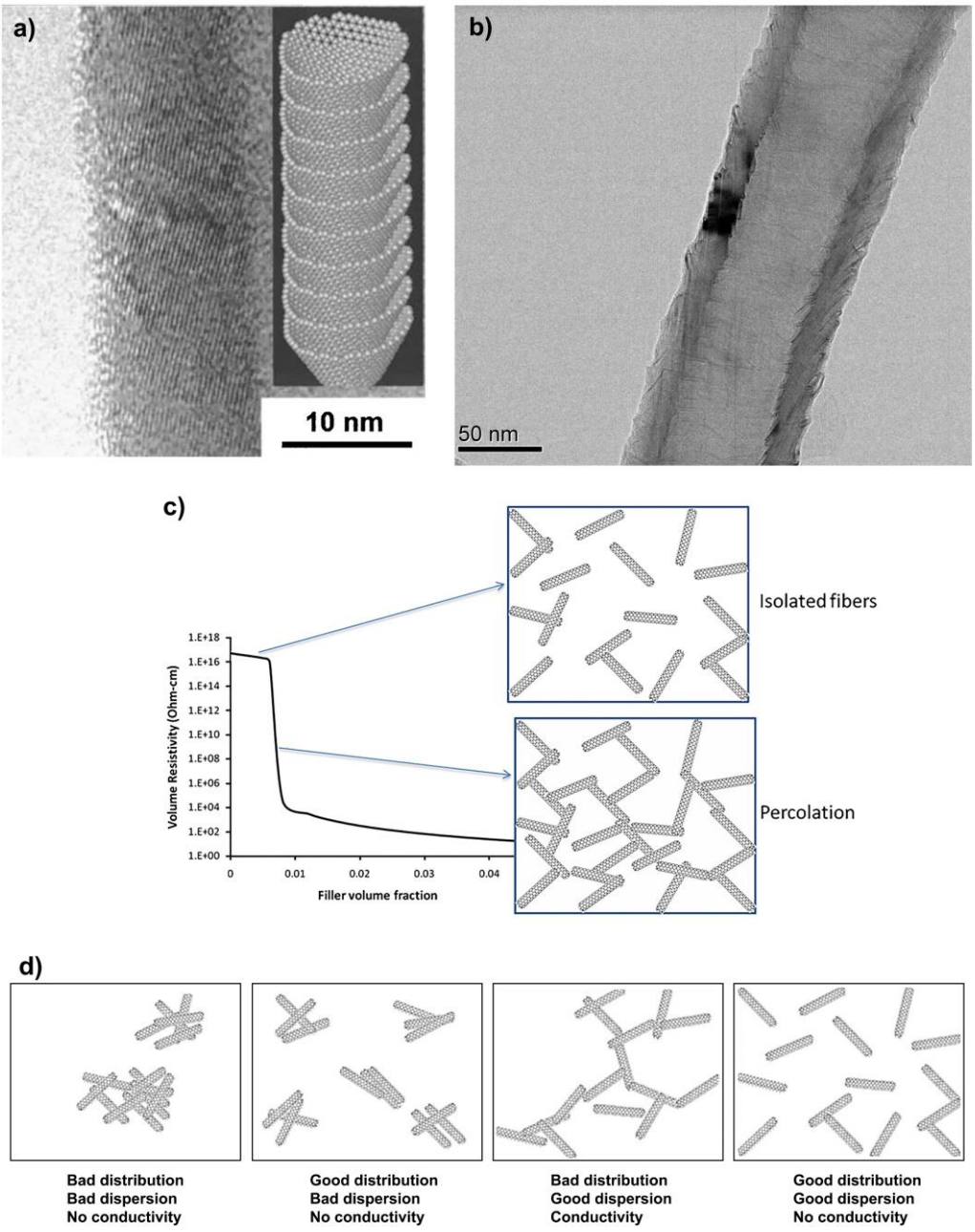

Figure 1.5. a) High resolution TEM image (inset shows the stack cone structure of a CNF) [78], b) TEM image of an individual CNF, c) electrical resistivity as a function of filler loading and d) schematics showing the effect of CNF distribution and dispersion on electrical conductivity inside an insulative matrix [69].

In this thesis, electrically conductive, porous SF/CNF nanocomposites were fabricated for tissue engineering applications. The specific aim of this thesis was the comprehensive investigation of the effects of SF/CNF nanocomposite characteristics (fibroin content, pore size, total pore volume and CNF concentration) on the physical and mechanical properties of scaffolds, as well as assessing their influence on the biological interactions of cells with the nanocomposites. In this thesis, a comprehensive design of an electrically conductive porous SF/CNF nanocomposite was carried out. Results indicated that SF/CNF nanocomposites could be potential candidates for tissue engineering applications, especially for applications where transmission of electrical impulses was a prerequisite for tissue regeneration.

CHAPTER 2

EXPERIMENTAL METHODS

2.1 Materials

Cocoons of *Bombyx Mori* were purchased from Kozabirlik (Bursa, Turkey). CNFs (<100 ppm iron content without surface functional groups), sodium carbonate (Na_2CO_3), lithium bromide (LiBr), 1,1,1,3,3,3-hexafluoro-2-propanol (HFIP) and methanol (CH_3OH) were purchased from Sigma Aldrich (St. Louis, Missouri) and used as received. NaCl particles were purchased from Isolab (Istanbul, Turkey). Dulbecco's Modified Eagle Medium (DMEM), penicillin-streptomycin, fetal bovine serum (FBS) and tyripsin-EDTA were purchased from Biosera (Nuaille, France). 3-(4,5-dimethyl-2-thiazolyl)-2,5-diphenyl-2H-tetrazolium bromide (MTT), dimethyl sulfoxide (DMSO), glutaraldehyde and hexamethyldisilizane (HMDS) were purchased from Glentham (Wiltshire, UK), Genaxxon Bioscience (Ulm, Germany), Merck (Darmstadt, Germany) and Sigma (St. Louis, Missouri), respectively. Ultrapure water prepared with a Millipore Milli-Q purification system (Burlington, Massachusetts) was used in all experiments.

2.2 Extraction of Silk Fibroin from the *Bombyx Mori* Cocoons

SF was extracted from *Bombyx Mori* cocoons. Sericin outer protein layer was dissolved by boiling cocoons in 0.02 M Na_2CO_3 solution for 30 min at 80 ^oC. The extracted SF was dried inside a fume hood for 12 hr. The dried SF was dissolved in 12 M LiBr solution for 4 hr at 60 ^oC and dialyzed against distilled water for 4 days to remove Li^+ and Br^- ions. Afterwards, dialyzed SF solution was centrifuged for 30 min at 4 ^oC to remove left-over impurities, followed by freezing the SF/water

solution at -20 ^{o}C for 24 hr. Finally, the frozen SF/water solution was lyophilized using Christ Alpha 2-4 LDplus. Lyophilized SF was stored at room temperature.

2.3 Scaffold Fabrication

To fabricate porous 3D fibroin scaffolds, HFIP was used as a solvent to dissolve lyophilized SF and NaCl particles were used as porogen agent. Firstly, SF was weighted to obtain 5 and 10 % (wt./v) HFIP/SF solutions. NaCl particles were sieved to obtain 50-90, 100-180 and 350-425 μm particle size ranges as per ASTM E1638 standard. Scaffolds fabricated using NaCl particles having 50-90, 100-180 and 350-425 μm size ranges (15:1 NaCl:SF ratio) were named as SF_50, SF_100 and SF_350, respectively. NaCl particles were weighted to obtain of 5:1, 10:1, 15:1, 20:1 and 25:1 NaCl:SF (wt.:wt). For convenience, the fabricated scaffolds were named as per NaCl:SF weight ratio utilized in their fabrication; for instance, 5Na:SF nomenclature was used for the NaCl:SF ratio of 5:1 and 25Na:SF was used for 25:1 ratio, etc. CNFs (with 50-70 nm inner diameter and 20-200 μm length) were incorporated into porous SF scaffolds at 0, 1, 3, 5, 7.5, 10 and 15 wt.% concentrations. For instance, 0.03 g CNFs were incorporated into 0.3 g SF for the nanocomposite having 10 wt. % CNF. In the fabrication of SF/CNF nanocomposite scaffolds, other fabrication parameters (5% SF, 350-425 μm NaCl particle size range and NaCl:SF ratio of 15:1) were kept constant. The SF/CNF nanocomposite scaffolds were named with a suffix identifying their CNF content; for instance, SF-0C nomenclature was used for 0% CNF and SF-1C nomenclature was used for 1% CNF, and etc. Prior to scaffold fabrication, CNFs were treated in 1:1 HNO_3:H_2SO_4 (v:v) solution for 24 hs (to obtain surface functional groups), thoroughly rinsed with DI water and dried inside an oven at 60 ^{o}C. SF was dissolved in as-received HFIP (for 0 wt. % CNF concentration) and HFIP/CNF mixtures to obtain 1, 3, 5, 7.5, 10 and 15 wt. % CNF concentrations. Afterwards, NaCl particles were incorporated inside HFIP/CNF/SF solution and placed inside a fume hood for another 24 hr to evaporate HFIP. Once HFIP evaporated, samples were placed in methanol for 24 hr to induce crystallization of

fibroin. Finally, the scaffolds were washed with DI water for 4 days to dissolve NaCl particles. Schematic drawing of the production route was given in Figure 2.1.

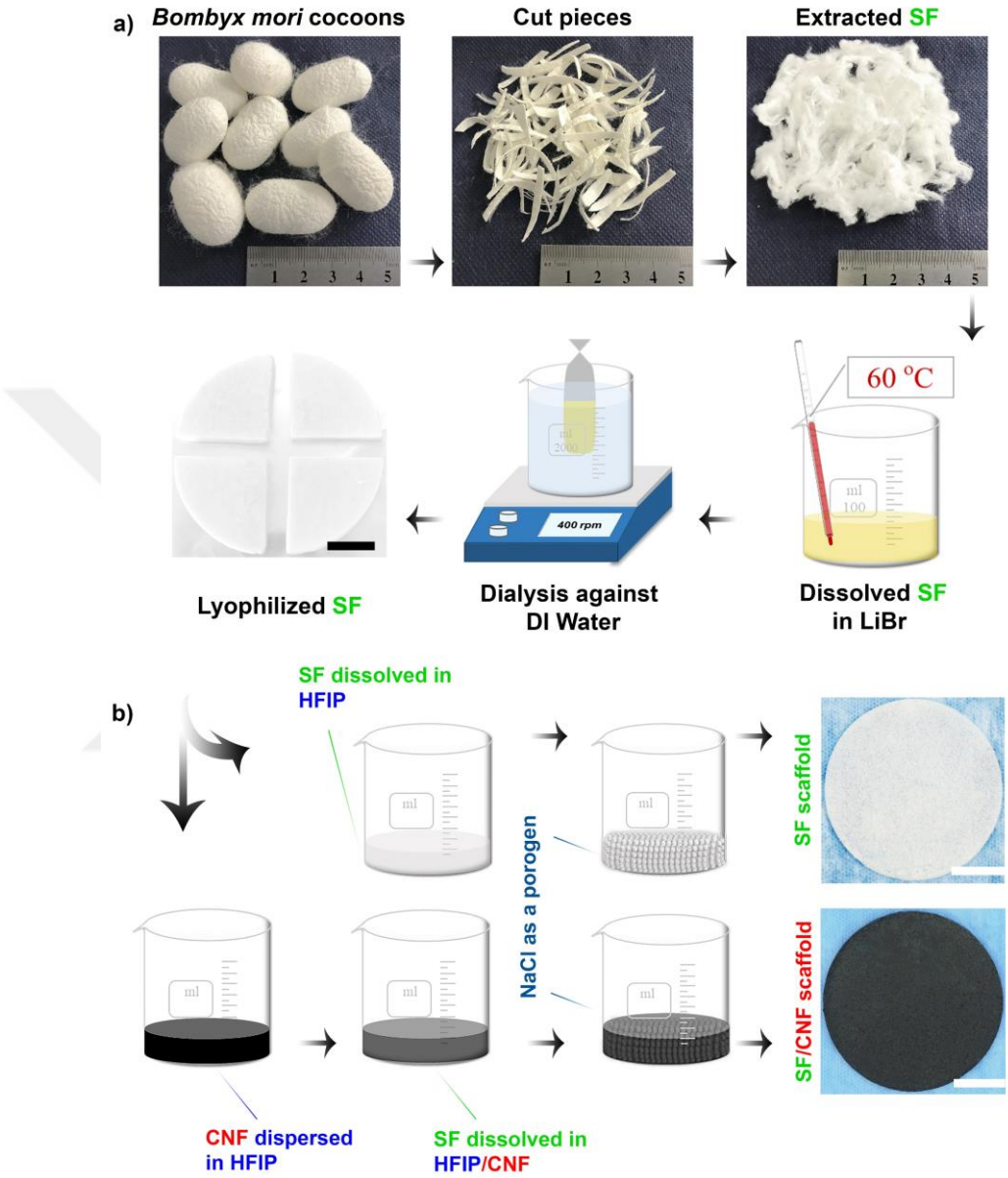

Figure 2.1. Schematic showing the fabrication steps of SF/CNF scaffolds. a) *Bombyx Mori* cocoons were cut and boiled in 0.02 M Na_2CO_3 solution to extract SF protein. Extracted SF was dissolved in 12 M LiBr solution, followed by dialysis against DI water. Afterwards, the dialyzed SF aqueous solution was lyophilized. b) Lyophilized SF was dissolved in CNF dispersed HFIP at 5% and 10% SF/HFIP (wt./v) concentrations (no CNF was used for the control samples). After that, NaCl particles

having different particle size ranges (50-90, 100-180 and 350-425 μm) were incorporated into SF/HFIP solution at 5:1, 10:1, 15:1, 20:1 and 25:1 (wt./wt.) NaCl:SF ratios. Finally, samples were rinsed with DI water to remove NaCl particles. Scale bars are 2 cm.

2.4 Characterization of SF/CNF Nanocomposite Scaffolds

2.4.1 Scanning Electron Microscopy (SEM)

FEI Nova Nano SEM 430 microscope (Brno, Czech Republic) was used to image cross-sections and fracture surfaces of the scaffold. Philips XL30 ESEM FEG (Eindhoven, Netherland) microscope was used to characterize cellular morphologies. Up to 10 kV accelerating voltage was utilized during image acquisition. Prior to SEM characterization, Quorum SC7640 high-resolution sputter coater (East Sussex, UK) was used to coat a thin gold layer on scaffolds to create an electrically conductive path.

2.4.2 Transmission Electron Microscopy (TEM)

CNFs were prepared for TEM characterization via ultrasonic dispersion in 2-propanol. 1 μl of this solution was dropped on a holey carbon coated copper grid and allowed to dry for 5 min. Micrographs were captured using high-resolution (HR) mode of FEI Tecnai G2 F30 TEM (Hillsboro, Oregon) at 200 kV accelerating voltage.

2.4.3 Atomic Force Microscopy (AFM)

For nanoscale roughness measurements, Veeco MultiMode (NY, US) atomic force microscope was used. Samples were examined under ambient condition using the tapping-mode. A silicon scanning probe (PointProbe-Plus, Nanosensors) with tip

apex cone angle of 10° and radius smaller than 7 nm was used for the measurements. 2 μm × 2 μm AFM fields from 3 different regions of SF/CNF nanocomposite films were analyzed and average root-mean-squared roughness (Rq) values were reported for each specimen.

2.4.4 Fourier Transform Infrared Spectroscopy (FTIR)

Lyophilized SF, porous SF and SF/CNF composite scaffolds were scanned in 4000-400 cm^{-1} range with 4 cm^{-1} resolution using PerkinElmer 400 Fourier transform infrared spectrometer (Waltham, Massachusetts) using attenuated total reflection (ATR) configuration. Background spectra were subtracted from the obtained reflectance data and the average of 4 spectra was reported for each sample. To identify the secondary structure of SF/CNF nanocomposite scaffolds the amide I region (1595-1705 cm^{-1}) was investigated by Origin 2019b software. Firstly, the second derivative was applied to the original spectra in the amide I region with a nine-point Savitsky-Golay smoothing filter so that the number and position of bands were determined [79][80]. Then, baseline was subtracted from the original band. For the curve fitting, Gaussian function was used. The deconvoluted spectra were area-normalized and the areas under the single bands were used to determine the fraction of the secondary structural elements [79][80].

2.4.5 X-ray Diffraction (XRD)

XRD patterns of lyophilized SF, CNF powders (before and after acid treatment), and SF/CNF nanocomposite scaffolds were obtained using Rigaku D/Max-2200 X-ray diffractometer (Tokyo, Japan) with monochromatic Cu Kα radiation (λ = 1.54 Å) at 40 kV. Diffraction angles (2θ) from 10° to 40° were scanned at a scanning rate of 2°/min.

2.4.6 Mechanical Properties

Mechanical properties of the scaffolds were characterized via uniaxial tensile testing (Instron 5565A, Norwood, MA). Tests were applied to 1 x 5 cm cut sheets (as per ASTM 638 standard) and the gauge length was kept constant at 2 cm in all experiments (Figure 2.2). A 0.1 mm/s loading rate was applied using a 5 kN load cell. Mechanical properties of the scaffolds were tested in wet condition at 37 ºC.

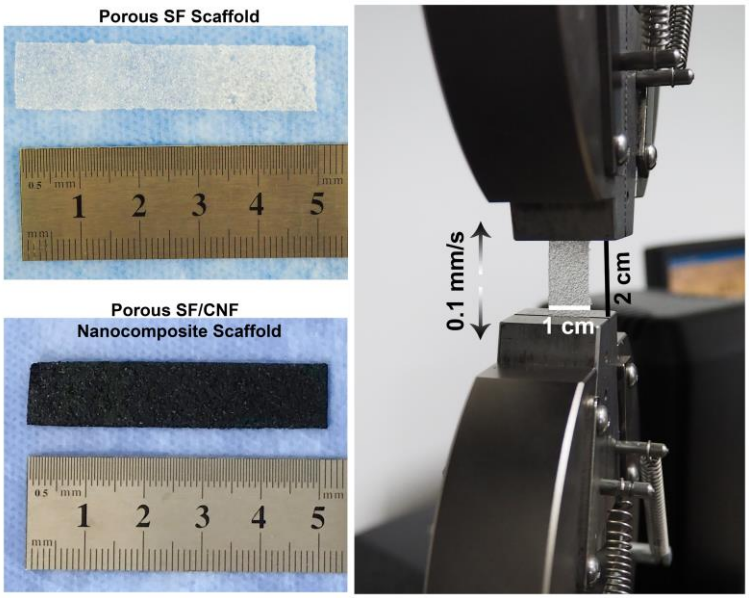

Figure 2.2. Uniaxial tensile testing

2.4.7 Micro-CT Analysis

The 3D microstructures of the SF scaffolds (2 cm x 2 cm) were investigated using computed tomography scans (Bruker MicroCT, Kontich, Belgium). 360° scans having 0.4 angular steps with 800 ms acquisition time per image were completed for the SF scaffolds. Al + Cu filter and 100 kV potential were used for imaging. Total pore volume calculations were carried out from three different segments of the scaffolds with 41 cross-sectional images per segment. Nrecon software was used to reconstruct the data, CTVox software was used for 3D visualization and CTAn software was used to analyse the data (Skyscan, Bruker).

2.4.8 Electrical Conductivity Measurements

For the resistance measurements of the scaffolds, the two-point probe method was utilized. A silver-based paste was applied onto the opposite sides of a strip shaped scaffolds. The resistivity values were calculated using the following equation (1):

$$\rho\ (ohm - cm) = (wtR)/l10 \qquad (1)$$

where w was the width and t was the thickness of the specimen, l was the distance between silver paste coatings and R was the measured resistance. Then, reciprocals of resistivity values were reported. Three specimens were measured for each sample and average values were reported.

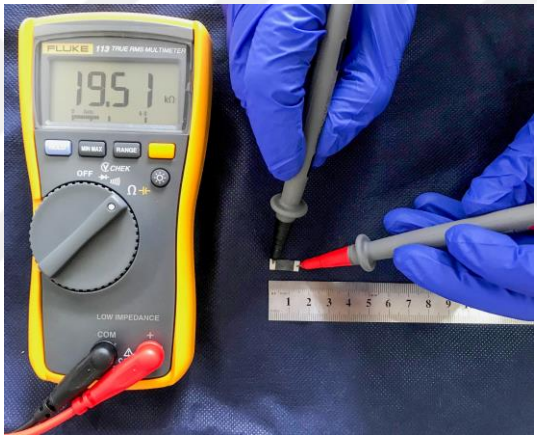

Figure 2.3. Electrical conductivity measurement

2.4.9 Water Contact Angle Measurements

To investigate the wettability of scaffold surfaces, water contact angles on SF films having various CNF concentrations were measured. Sessile drop water contact angle measurements were conducted using Attension Theta equipment (Gothenburg, Sweden). The contact angles of 7 µl distilled water droplets were measured 5 seconds after they were introduced on SF/CNF films. The experiments were repeated in triplicate with 3 different measurements for each sample.

2.4.10 Cell Culture and Metabolic Activity

Prior to the experiments, scaffolds were sterilized with 70% ethanol and UV radiation each for 15 min, followed by incubation in DMEM containing 5% (v/v) penicillin/streptomycin for 3 days. *In vitro* cell culture experiments were conducted with L929 mouse fibroblast cells (ATCC NCTC clone 929, passage number 18) using complete growth medium containing High Glucose DMEM supplemented with FBS (10% (v/v)) and penicilin-streptomycin (1% (v/v)). Cells were cultured inside a humidified incubator at 37 ^{o}C and 5% CO_2. Metabolic activities of fibroblasts on SF scaffolds were investigated using MTT assay. Sterile samples were seeded with L929 cells at a density of 3500 cells/cm^2. After culturing the cells on the scaffolds for 4 hr, 1, 3 and 5 days *in vitro* under standard cell culture condition (37 ^{o}C, 5% CO_2), culture media on the scaffolds were aspirated and 150 µl of complete growth medium containing 10% (v/v) MTT reagent was added to further incubate for 3.5 hr. At the end of 3.5 hr, MTT solution was removed and 100 µl of DMSO was added into each well to dissolve the formazan crystals formed by viable cells. 75 µl of the solution containing dissolved formazan was transferred and its absorbance was recorded using Microplate Absorbance reader (iMark Microplate Absorbance Reader, BioRAD, CA, US) at 570 nm (reference wavelength-750 nm). The absorbance values of blank samples without any cells were subtracted from the obtained absorbance values. The number of cells adherent on each sample was determined by comparing the absorbance values to a standard curve constructed at the beginning of each trial. Cell proliferation experiments were repeated in triplicate.

2.4.11 Statistical Analysis

All experiments were performed in triplicate and the results were represented as mean ± standard deviation (SD). Statistical analyses were performed with one-way analysis of variance (ANOVA) using Tukey's post hoc test with significance based on $p < 0.05$.

CHAPTER 3

RESULTS AND DISCUSSION

The rationale behind this study was to fabricate electrically conductive porous SF/CNF nanocomposite scaffolds having optimum mechanical and electrical properties and biological interactions. For this purpose, four different fabrication parameters were optimized via detailed scaffold characterization, namely i) NaCl particle size, ii) NaCl:SF (w:w) ratio, iii) SF concentration and iv) CNF concentration. The effect of each fabrication parameter on the scaffold properties was examined individually under the following headings.

3.1 Effect of Porogen Size on SF Scaffold Properties

Micro-CT and cross-sectional SEM images of the scaffolds fabricated using NaCl particles with different size ranges were provided in Figure 3.1. When the size range of NaCl particles was 50-90 μm, an average pore size of 67 ± 15 μm was obtained (Figure 3a and h) and a distinct film-like skin layer formed on the surface during solvent evaporation (Figure 3.1a) [17][81]. On the other hand, larger pores having an average size of 118 ± 24 μm were obtained for SF_100, as evident in Figure 3.1d. Distinct pores and pore boundaries were apparent in the frontal and cross-sectional micro-CT images of SF_100 (Figure 3.1b). Similar to SF_50, a skin layer was also observable in the cross-sectional micro-CT image of SF_100. Further increase in the NaCl particle size to 350-425 μm yielded a more open microstructure within the SF scaffolds, as shown in Figure 3.1c, having an average pore size of 376 ± 53 μm (Figure 3.1d). Pore volume analysis from Micro-CT images revealed a proportional increase in the total pore volume with an increase in NaCl particle size. NaCl particles having a size range of 50-90 μm generated a total pore volume of 0.15 ±

0.01 mm^3, while the total pore volumes were calculated to be 0.40 ± 0.02 mm^3 and 0.58 ± 0.07 mm^3 for SF_100 and SF_350, respectively (Figure 3.1e).

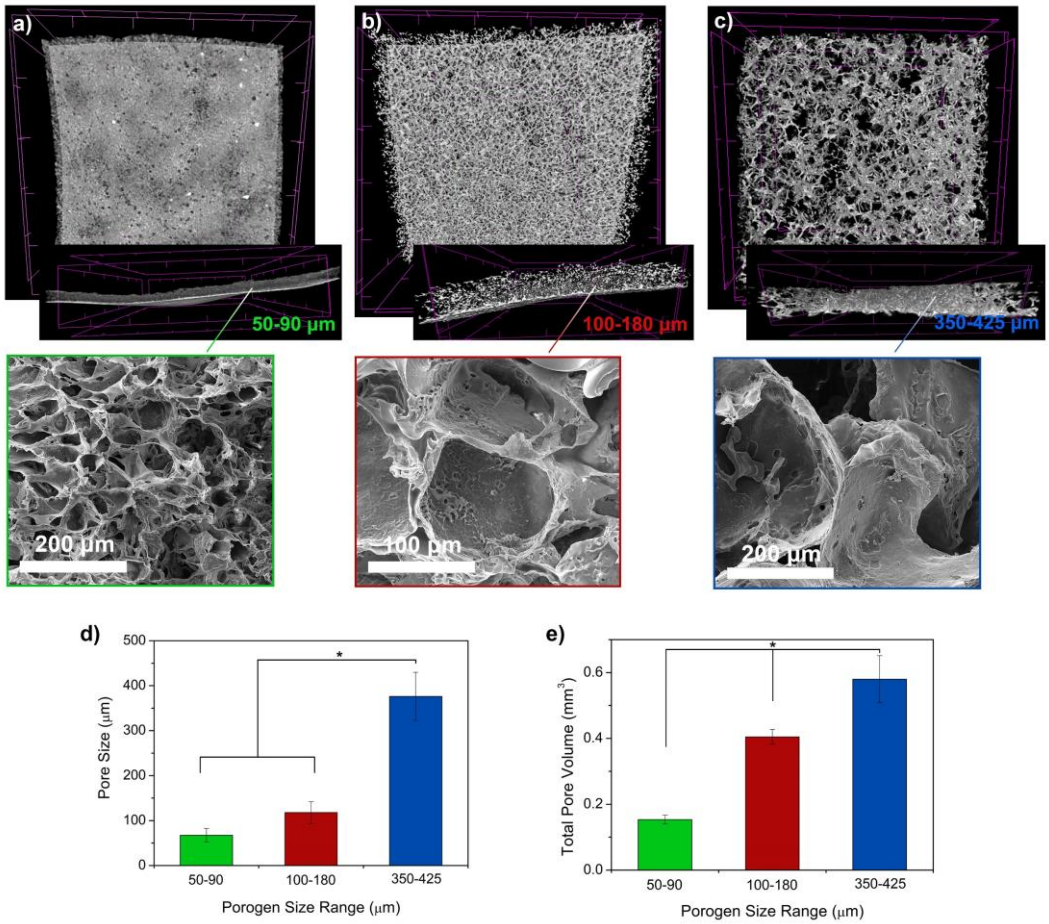

Figure 3.1. (a-c) Micro-CT and SEM images of SF scaffolds fabricated using a) 50-90, b) 100-180 and c) 350-425 µm NaCl particle size range, d) pore sizes and e) total pore volumes of SF_50, SF_100 and SF_350. *$p < 0.05$.

As evident in micro-CT and SEM images, NaCl particles transferred their shapes and provided uniform porous architectures across the SF scaffolds independent of the NaCl particle size. Therefore, control on the pore size, as well as the total pore volume was achieved solely through the adjustment of NaCl particle size for SF scaffolds, which in turn, altered scaffold properties. During scaffold fabrication, an equal amount of SF was used to fabricate SF_50, SF_180 and SF_350, which manifested itself as an increase in the volume of the scaffolds. The increase in

scaffold volume, in turn, increased the thickness of the scaffolds, *i.e.* SF_50 was thinner and had a compact appearance compared to SF_180 and SF_350 as evident in their cross-sectional micro-CT images. Since equivalent amounts of NaCl particles were utilized in the fabrication of scaffolds, the volume expansion upon the use of larger NaCl particles could be attributed to the increased packing density of smaller NaCl particles, which led to less entrapped air between NaCl crystals and SF/HFIP solution during scaffold fabrication.

Uniaxial tensile testing showed that the tangent modulus values of the scaffolds exhibited an inverse proportionality with mean pore size (Figure 3.2a). Specifically, the tangent modulus was calculated to be 50 ± 10 kPa for SF_350 and it increased to 90 ± 40 kPa for SF_100 and 230 ± 30 kPa for SF_50 (Figure 3.2b). SEM images taken from the tensile fracture surfaces revealed characteristic fracture surface of SF without any noticeable difference with changes in scaffold pore size range (Figure 3.2c, d and e).

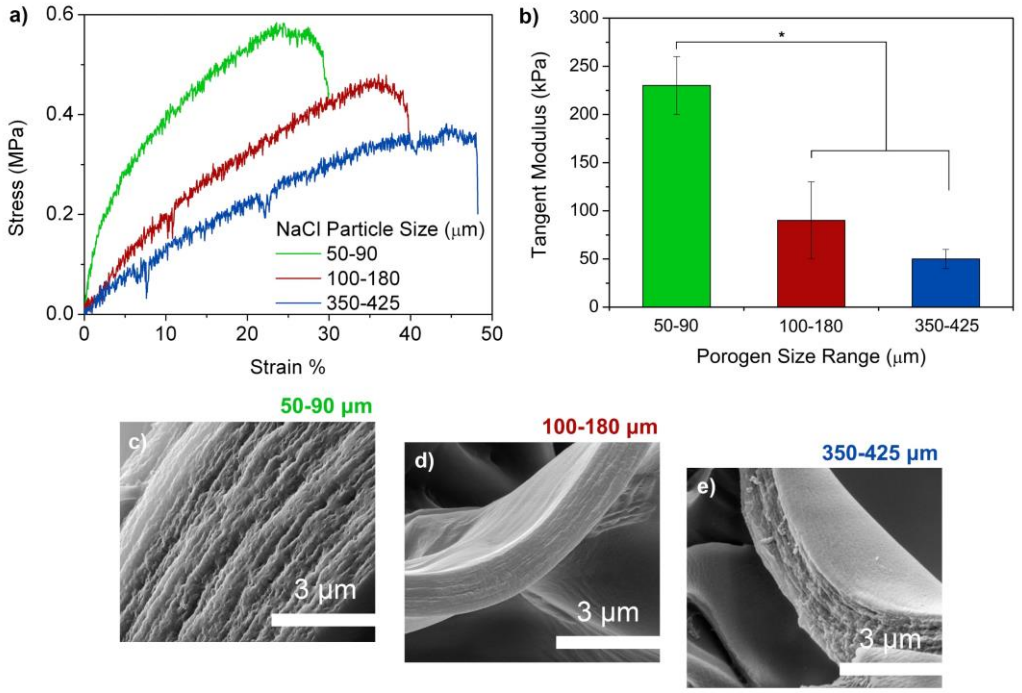

Figure 3.2. a) Stress-strain curves and b) tangent modulus values of SF_50, SF_100 and SF_350, (c-e) fracture surfaces of scaffolds prepared using c) 50-90, d) 100-180 and e) 350-425 μm NaCl particle size range. *$p < 0.05$.

Formation of β-sheet crystallites was confirmed through FTIR-ATR analyses of the scaffolds (Figure 3.3). Silk I (random coils+α-helices) peaks obtained at ~1640 and ~1530 cm^{-1} for L_SF shifted to ~1620 and ~1510 cm^{-1} for SF_100 and SF_350 suggesting the formation of β-sheet crystallites [81][82]. It is interesting to note that silk II peaks appeared at ~1624 and ~1516 cm^{-1} in the spectra of SF_50. The larger peak shift (from silk I structure to silk II structure) for SF_100 and SF_350 compared to that of SF_50 indicated better interaction of methanol with SF_100 and SF_350 due to the increase in porosity of the scaffolds (total porosities of SF_50, SF_180 and SF_350 were found to be 57%, 66% and 78%, respectively). Still, it should be noted that more intense β-sheet crystallite peaks were obtained in the spectra of SF_350 compared to SF_100, which highlighted the enhanced interaction efficacy of methanol with SF_350 due to having ~45% more pore volume compared to SF_100. It was also confirmed through deconvolution of amide I regions in the FTIR spectra of L-SF, SF_50, SF_100 and SF_350 (Figure 3.3b, 3.3c, 3.3d and 3.3e, respectively) [79][80]. Results indicated that β-sheet content of L-SF was increased from 23.2% to 31.9%, 36.8% and 39.1% for SF_50, SF_100 and SF_350, respectively. On the other hand, tangent modulus and mean pore size of scaffolds were found to be inversely proportional, which was in-line with composite theory and literature findings [28]. As the NaCl particle size range increased, so did the mean pore size and the porosity. The increased porosity of the scaffolds, which acted as void regions in the microstructure, led to the decreased load bearing capacity of the SF scaffolds.

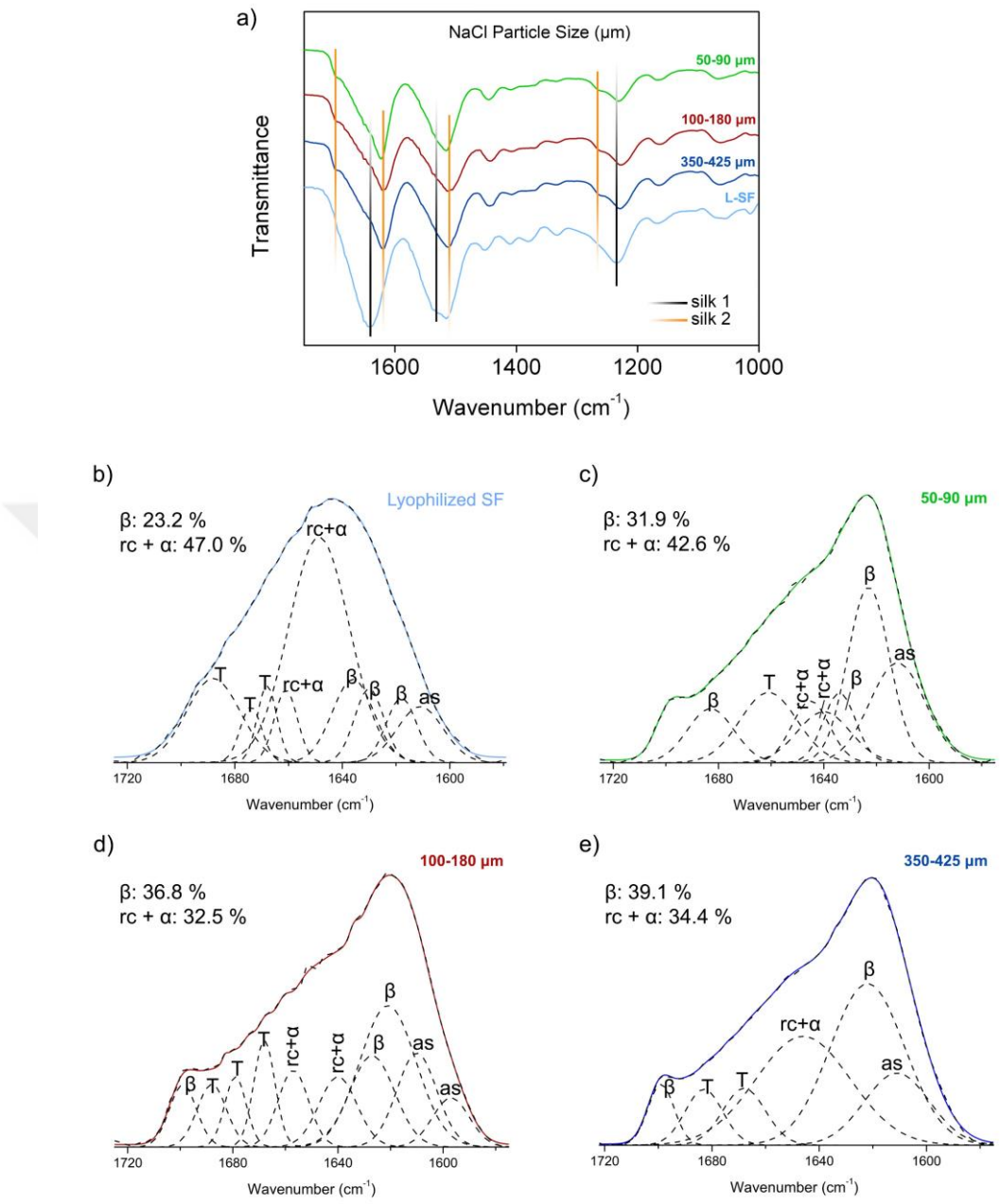

Figure 3.3. a) FTIR spectra of scaffolds prepared using different 50-90, 100-180 and 350-425 µm NaCl particle size ranges and L-SF, (b-e) fractions of secondary structural elements obtained from the deconvolution of amide I regions of b) L-SF and SF scaffolds fabricated using NaCl particles in the size ranges of c) 50-90 µm, d) 100-180 µm and e) 350-425 µm. β: β-sheets, T: β-turns, rc+α: random coils + α-helix and as: aggregated strands.

The effect of porogen size on the biological properties of scaffolds were assessed using fibroblast cells. MTT assay results revealed that cell densities did not show any statistically significant difference between SF_50 and SF_100 at 4hr and 1 day *in vitro*, whereas more cells were present on SF_100 after the 3rd day of culture (Figure 3.4). On the other hand, fibroblasts adhered and proliferated more on SF_350 compared to its counterparts with smaller pores. In fact, fibroblast densities on SF_350 was the highest on all investigated time points owing to its open structure that facilitate the infiltration of cells, while providing more space for cells to proliferate. In brief, NaCl particles in the size range of 350-425 µm provided enhanced cell adhesion and proliferation together with a tangent modulus of 50±10 kPa that was similar to that of cardiac tissue [11]. Therefore, 350-425 µm particle size range was chosen as the optimum porogen size in the fabrication of porous SF/CNF nanocomposite scaffolds.

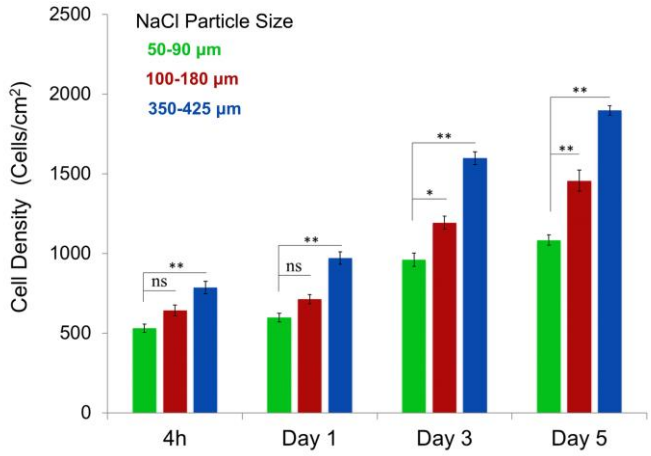

Figure 3.4. Fibroblast cell densities up to 5 days of culture on scaffolds prepared using different 50-90, 100-180 and 350-425 µm NaCl particle size ranges. *$p < 0.05$, **$p < 0.001$.

3.2 Effect of Porogen Content on SF Scaffold Properties

Aside from NaCl particle size, the amount of NaCl utilized in the fabrication of SF scaffolds also had a significant role on the design of optimum porous architecture.

The micro-CT images and the visual appearances of scaffolds containing the lowest (5Na:SF) and the highest (25Na:SF) amount of NaCl were provided in Figure 3.5a and 3.5b. 25Na:SF revealed a sponge-like appearance with homogeneously distributed pores throughout its volume, while inhomogeneities in the structure of 5Na:SF (indicated with arrowheads) was evident with regions having less porous architecture. The total pore volumes of 5Na:SF and 25Na:SF were calculated as 0.36±0.03 mm^3 and 0.66±0.06 mm^3, respectively, suggesting an ~80% increase in the total pore volume upon the increase in NaCl:SF ratio from 5:1 up to 25:1 (Figure 3.5c). As evident in visual inspection and micro-CT images, for the 5Na:SF scaffolds the amount of NaCl particles was insufficient to generate a uniform porous structure, *i.e.* a portion of the SF in the solution remained less porous compared to other parts of the scaffold after the evaporation of HFIP as indicated with the arrowheads in Figure 3.5a. On the other hand, when NaCl amount was increased 5 folds to obtain 25:1 NaCl:SF ratio, a uniform porous architecture was obtained throughout the scaffold. Similarly, visual examination and micro-CT analysis of 15Na:SF (given in the fabrication scheme of Figure 2.1b and Figure 3.1c, respectively) revealed a uniform geometry having homogeneously distributed pores across the scaffold. Micro-CT results revealed that the total pore volume for 15Na:SF and 25Na:SF were found to be ~1.6 and ~1.8 times higher than that of 5Na:SF. Since the same amount of SF was utilized in the fabrication of these scaffolds, the total scaffold volume (pore volume and SF volume) of 25Na:SF was the highest, and thus had a more spongy appearance.

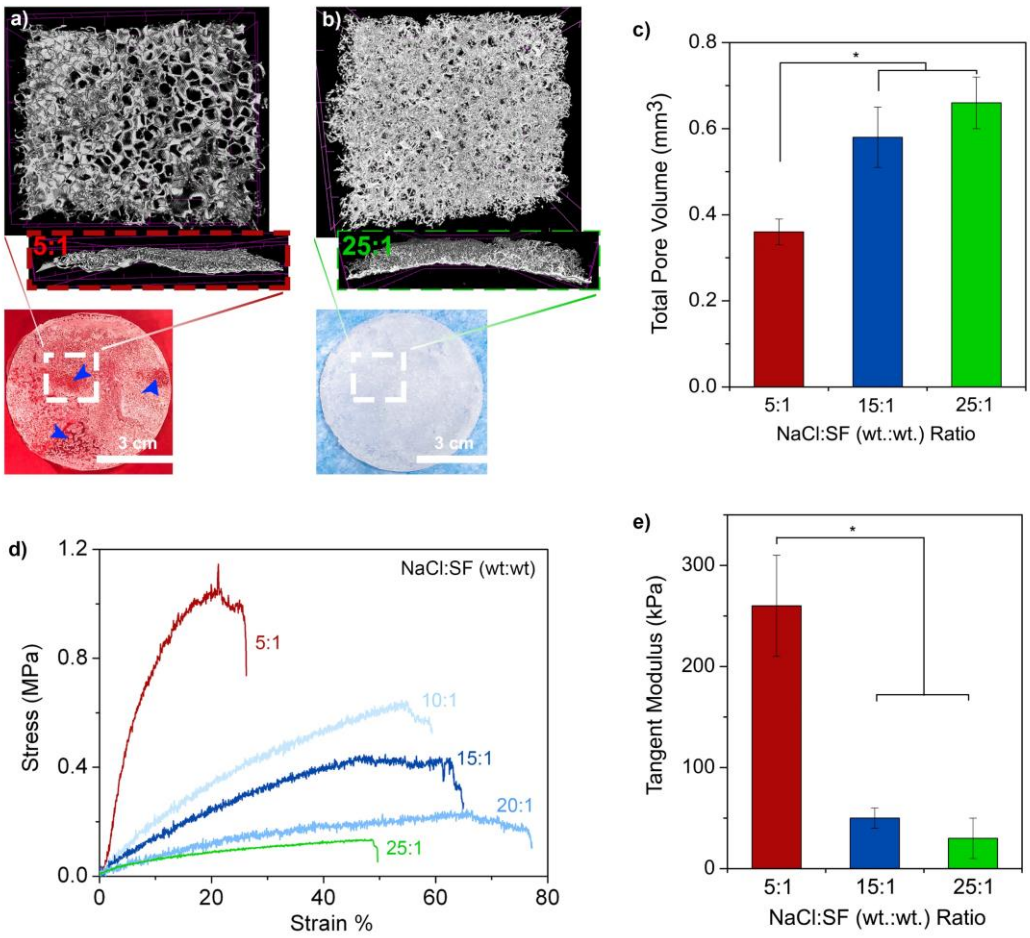

Figure 3.5. (a-b) Micro-CT and macro images of the SF scaffolds fabricated using a) (5:1) and b) (25:1) NaCl:SF ratios, c) total pore volume values, d) Stress-strain curves and e) tangent modulus values of SF scaffolds fabricated with various NaCl:SF ratios. *$p < 0.05$.

In Figure 3.6a, the FTIR spectra of scaffolds fabricated using NaCl:SF ratios of 5:1, 15:1 and 25:1 were compared with lyophilized SF (L-SF). For all SF scaffolds, peaks were observed at ~1620, ~1510 and ~1265 cm^{-1} for amide I, amide II and amide III regions, respectively, suggesting the formation of β-sheet crystallites [82][81]. However, peak intensities varied between individual scaffolds where more intense peaks were observed for 25Na:SF and 15Na:SF compared to 5Na:SF. Also, secondary structural elements of 5Na:SF, 15Na:SF and 25Na:SF were quantified through the deconvolution of amide I regions in their FTIR spectra (Figure 3.6b, 3.6c

and 3.6d, respectively). Results indicated that the 5Na:SF had the lowest β-sheet content (18.8%) and the highest amount of silk I structure (43.8%) compared to 15Na:SF and 25Na:SF. Also, comparing the secondary structures of 15Na:SF and 25Na:SF, the β-sheet content of the former is lower than the latter. This could be correlated with more open structures of 15Na:SF and 25Na:SF compared to 5Na:SF, which provided better methanol penetration into these scaffolds.

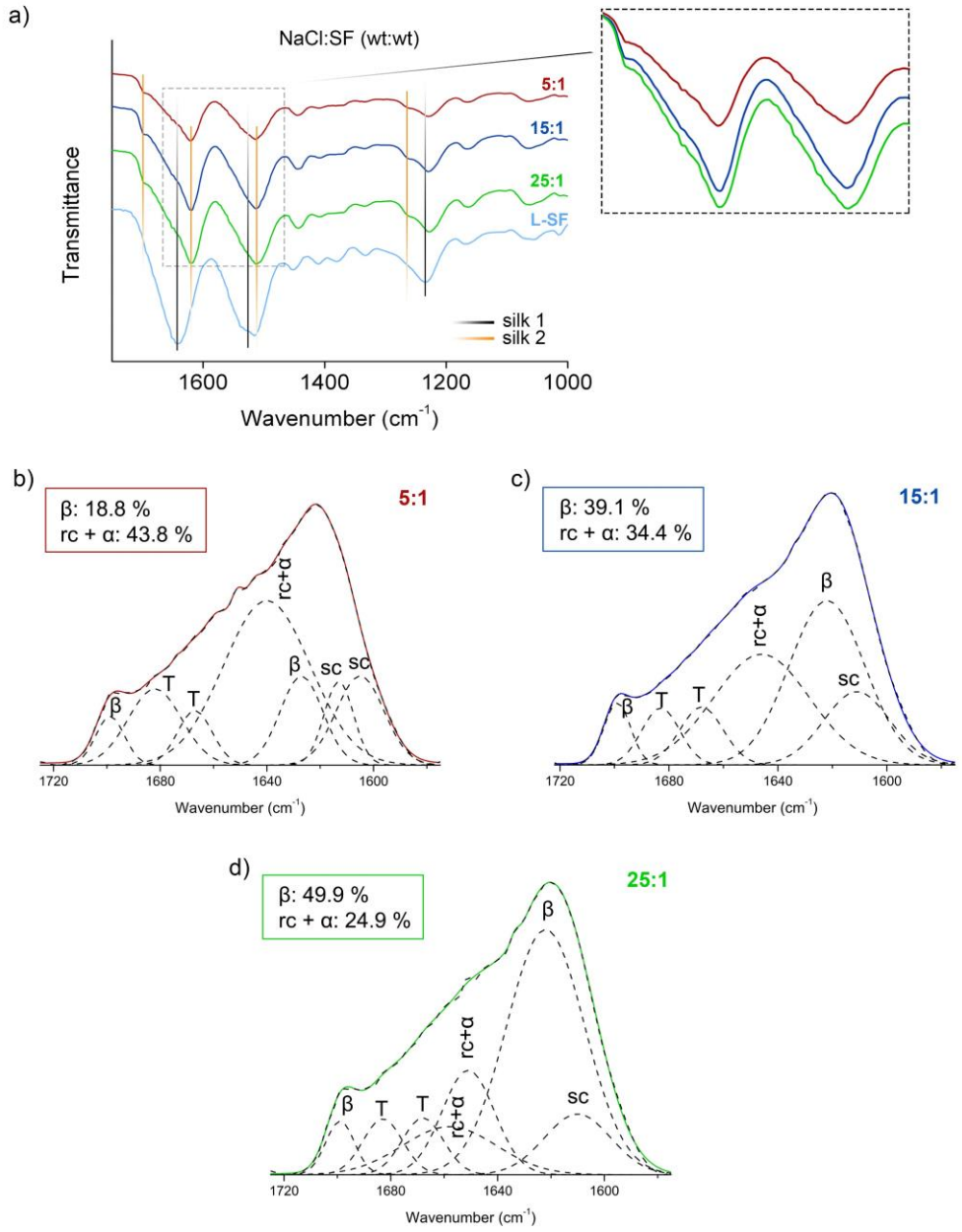

Figure 3.6. a) FTIR spectra of L-SF and SF scaffolds prepared using 5:1, 15:1 and 25:1 NaCl:SF ratios (wt.:wt.), (b-d) fractions of secondary structural elements obtained from the deconvolution of amide I regions of b) 5Na:SF, c) 15Na:SF and d) 25Na:SF. β: β-sheets, T: β-turns, rc+α: random coils + α-helix and as: aggregated strands.

These findings were in-line with the MTT assay results of scaffolds. L929 fibroblast densities on 5Na:SF, 15Na:SF and 25Na:SF up to 5 days of culture revealed that cellular adhesion on 15Na:SF and 25Na:SF were comparable after 4 hr of culture (Figure 3.7). However, fibroblast adhesion on 5Na:SF was lower compared to 15Na:SF and 25Na:SF. At all time points, cellular density on 25Na:SF was the highest, while similar densities were observed for 15Na:SF and 5Na:SF scaffolds.

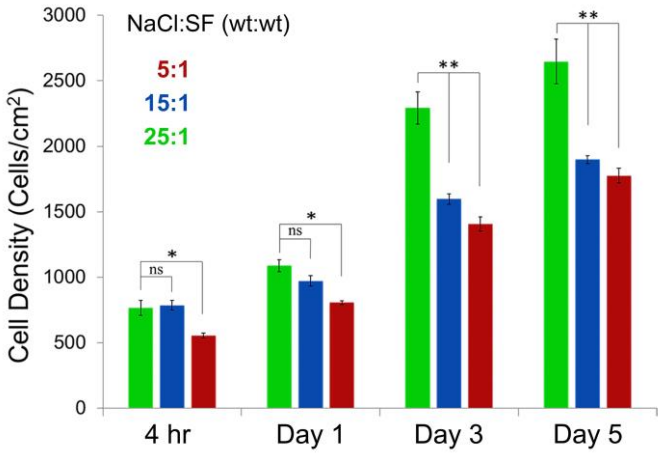

Figure 3.7. Fibroblast densities on SF scaffolds prepared using 5:1, 15:1 and 25:1 NaCl:SF ratios (wt.:wt.). *p < 0.01, **p < 0.0001.

Cumulatively, 5Na:SF had the highest and 25Na:SF had the lowest modulus values. On the other hand, highly open structure of 25Na:SF increased cellular proliferation compared to 15Na:SF and 5Na:SF. These results indicated that 15:1 NaCl:SF ratio had a microarchitecture that offered optimized mechanical properties and still promoted cellular proliferation for tissue engineering applications.

3.3 Effect of SF Concentration on SF/CNF Nanocomposite Scaffolds

The effect of SF concentration on scaffold properties was investigated through the fabrication of porous SF/CNF nanocomposites (with 0 and 5% CNF) having 5 and 10% SF concentrations. Other fabrication parameters including NaCl particle size (350-425 μm) and NaCl:SF ratio (15:1, wt.:wt.) were kept constant to compare the effect of SF concentration alone on the scaffold properties. Stress-strain curves of

SF5, SF10, SF5/5 and SF10/5 were given in Figure 3.8a. The tangent modulus values (Figure 3.8b) calculated as per ASTM E111 standard for SF5 and SF10 were 50±10 and 70±20 kPa, respectively, and did not indicate a statistically significant difference ($p>0.1$). In addition, the tangent modulus values for SF5/5 and SF10/5 were calculated to be 100±20 kPa and 80±40 kPa, respectively. SEM investigation of the fracture surfaces showed the pull-out regions and CNFs (highlighted with arrowheads) for SF5/5 and SF10/5 in Figure 3.8c and 3.8d, respectively. A statistically significant increase ($p<0.05$) in tangent modulus was evident for SF5 upon the addition of 5% CNF, while no statistically significant improvement was present ($p>0.1$) when the same amount of CNFs were incorporated into 10% SF. In comparison, the tangent modulus values of SF5/5 and SF10/5 exhibited similar values which further confirmed that the change in SF concentration did not lead to any significant difference ($p>0.1$) on the tangent modulus values of the scaffolds.

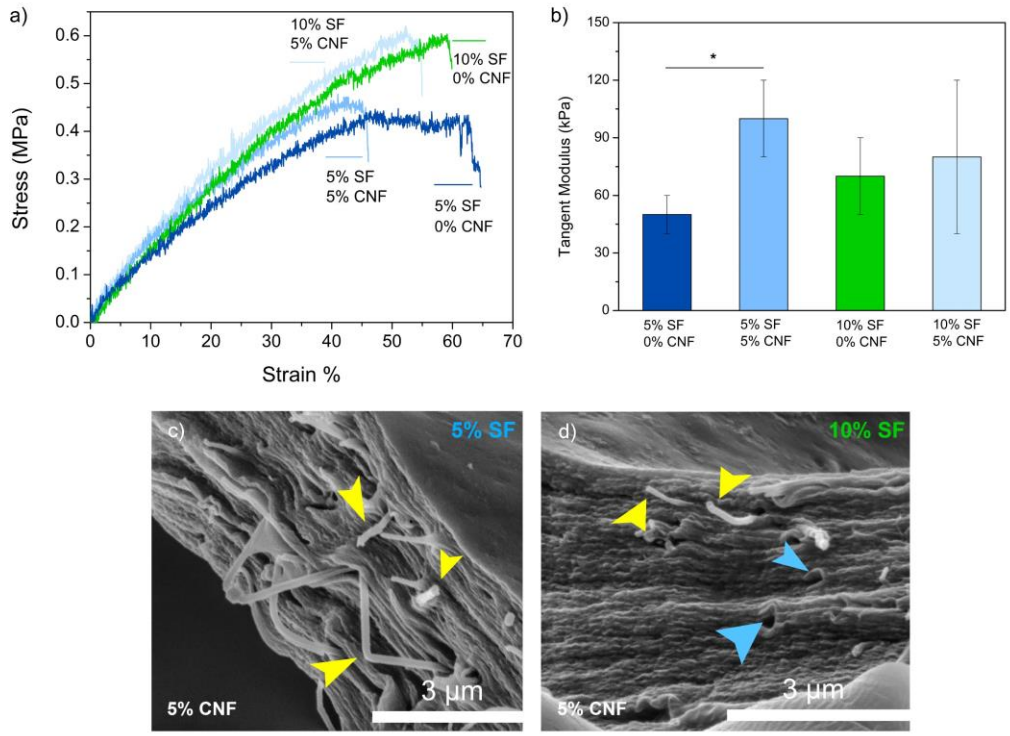

Figure 3.8. a) Stress-strain graphs and b) tangent modulus values for 5 and 10 % SF scaffolds upon incorporation of 5 % CNFs, (c-d) Fracture surfaces of c) SF5/5 and d) SF10/5 scaffolds. *$p < 0.05$.

This result could be explained with the differences in the FTIR (Figure 3.9a) peaks of the scaffolds. During scaffold fabrication, both SF5 and SF10 were exposed to methanol, yet more intense β-sheet crystal peaks were observed for SF5 despite having less fibroin. Also, deconvolution of amide I regions in the FTIR spectra of SF10 and SF5 (Figure 3.9b and 3.9c, respectively) revealed that the β-sheet content of SF5 (39.1%) was higher than that of SF10 (27.0%). This was an indication of better methanol penetration into the scaffold, which in turn enhanced β-sheet formation for SF5. One can speculate that although SF10 had more fibroin to withstand the applied stress, SF5 had higher crystallinity, which led to similar tangent modulus values for SF5 and SF10.

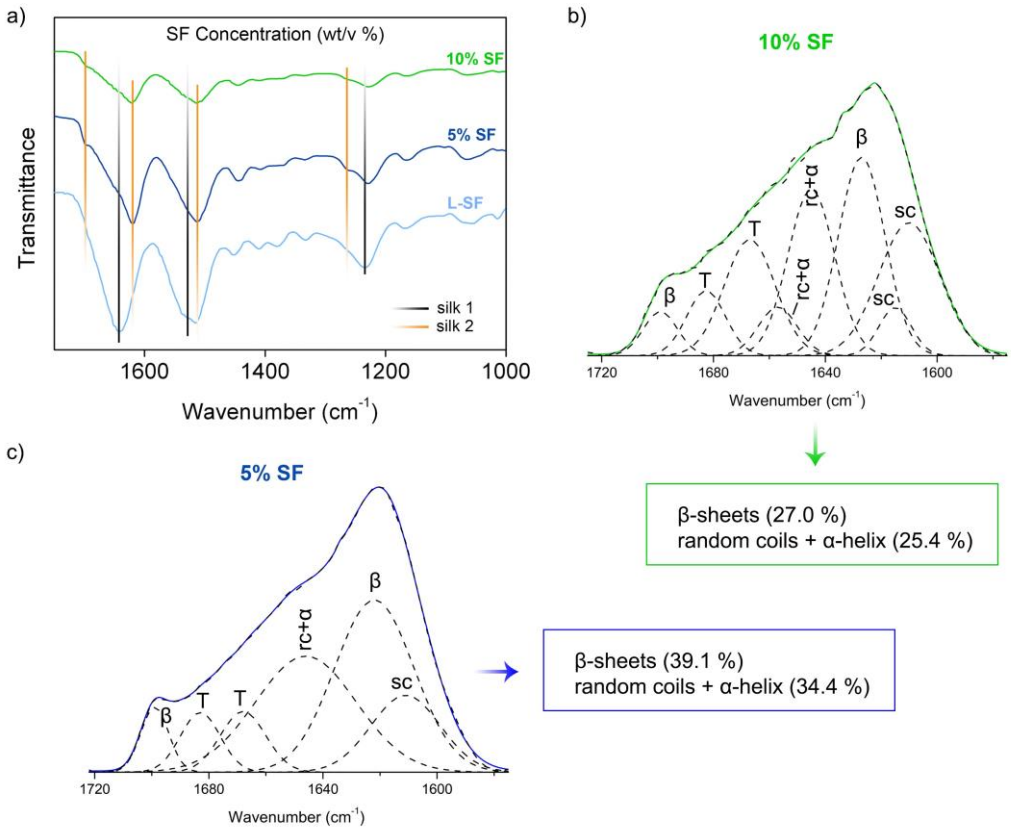

Figure 3.9. a) ATR-FTIR spectra of lyophilized SF (L-SF), SF5/5 and SF10/5 scaffolds, (b-c) fractions of secondary structural elements obtained from the deconvolution of amide I regions of b) SF10 and c) SF5. β: β-sheets, T: β-turns, rc+α: random coils + α-helix and as: aggregated strands.

Upon the incorporation of CNFs, electrical conductivities of SF5/5 and SF10/5 increased up to ~0.002 and ~5.5x10^{-5} S/cm, respectively (Figure 3.10a). Very low electrical conductivity of SF10/5 compared to that of SF5/5 could be attributed to the accumulation of CNFs into bundles inside SF10/5. The presence of CNF bundles on pore surfaces for SF10/5 were confirmed via cross-sectional SEM image given in Figure 3.10b (yellow boxes). Therefore, >35 times higher conductivity of SF5/5 compared to SF10/5 could be correlated with better dispersion of CNF within the SF matrix. Aside from having a higher viscosity, dissolution of SF in HFIP took a longer time for SF10 than SF5, which provided enough time for CNFs to form bundles (Figure 3.10b). The effect of CNF bundling for SF10/5 was also evident in the

mechanical properties of the scaffolds. The enhanced tangent modulus of SF5/5 further confirmed better dispersion of CNFs in SF5 compared to SF10, which led to an effective load transfer from the SF matrix to CNFs. In brief, the SF concentration did not change the tangent modulus of the scaffolds, yet 5% SF had a higher tendency to form β-sheet crystallites and had superior electrical conductivity. Therefore, 5% SF concentration was preferred for the fabrication of SF/CNF nanocomposite scaffolds.

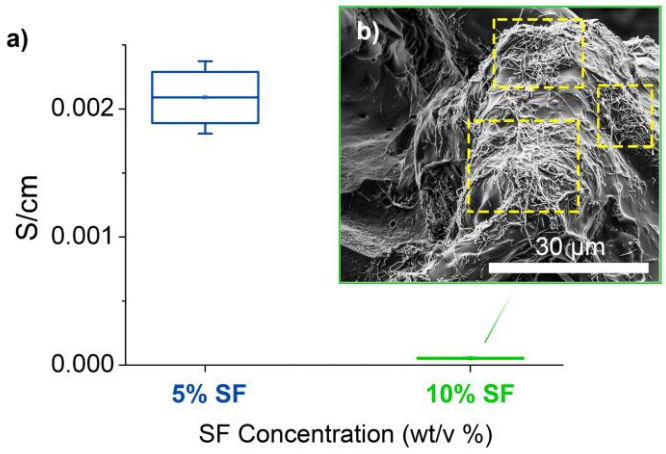

Figure 3.10. a) Electrical conductivities of SF5/5 and SF10/5 scaffolds and b) SEM image showing the CNF bundling on 10 % SF scaffolds.

MTT assay results up to 5 days of culture (Figure 3.11) confirmed that cells were viable and able to proliferate on both SF5 and SF10. Comparison of the adhesion (4hr) and proliferation of cells on the scaffolds did not yield any significant difference up to 5 days of culture. Adherent cells at the 3rd day of culture (dashed boxes in Figure 3.11) revealed round cellular morphologies with cells expressing filopodia on both scaffold surfaces. Cellular spreading on SF5 and SF10 were quantified to be 96.7 ± 20.4 and 117.0 ± 20.1 µm^2, respectively, indicating that cells could spread equally-well on both scaffolds independent of the SF concentration.

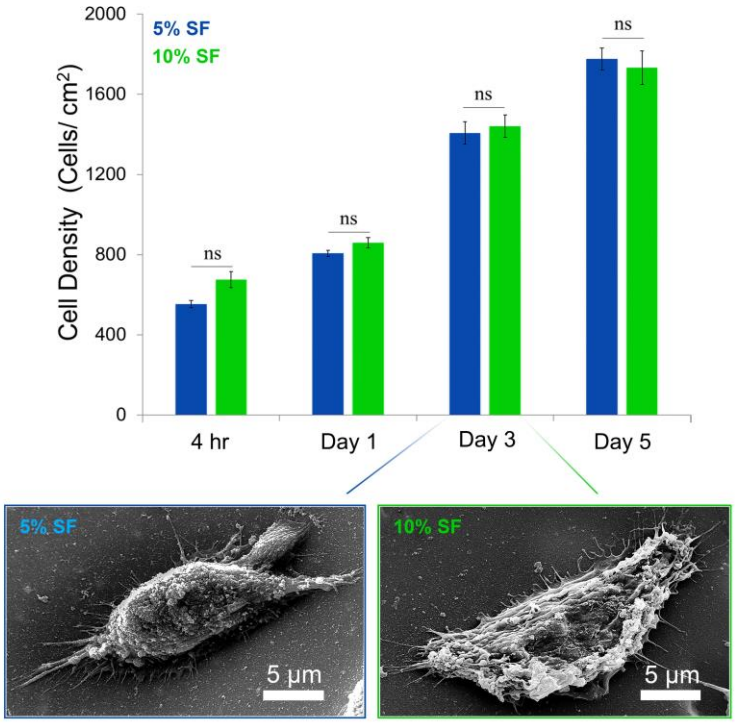

Figure 3.11. Cell densities on 5 and 10 % SF scaffolds up to 5 days of culture and the corresponding SEM images of fibroblasts cultured on these scaffolds.

3.4 Effect of CNF Concentration on SF/CNF Nanocomposite Scaffolds

The hollow microstructure of CNFs was evident in SEM and TEM images, as shown in Figure 3.12a and 3.12b, respectively. The CNFs used to fabricate the nanocomposite scaffolds were acid treated to obtain surface functional groups prior to incorporation into the SF matrix. Figure 3.12c showed the typical XRD patterns of CNFs (sharp (002) diffraction peak) for both as-received and acid functionalized CNFs (F-CNFs), indicating that there was no significant effect of the acid treatment on the crystalline structure of graphite layers [83]. Changes in the FTIR spectrum of CNFs after the acid treatment (Figure 3.12d) were in-line with literature where the intensive band of the as-received CNFs at 3434 cm^{-1} (mainly due to stretching vibrations of –OH in carboxyl group and adsorbed water) shifted to lower wavenumbers [84][85], while the peaks at 1735 and 1630 cm^{-1} could be attributed to

the C=O groups in carboxylic acid surface groups of the F-CNFs [86]. In addition, peaks at 1350, 1161 and 1068 cm^{-1} could be assigned to O-H bending and C-O stretching in aromatic carboxylic acids formed on CNFs after the acid treatment [85][86][87]. The effect of acid treatment on the dispersion efficacy of CNFs in both DI water and HFIP was visually examined (Figure 3.12e) and better dispersion of F-CNFs compared to the as-received counterparts was observed after a 20 min. ultrasonic dispersion. In addition, comparison of CNF dispersion in HFIP and DI water showed that HFIP better supported the dispersion of CNFs (especially the F-CNFs) compared to DI water, which was beneficial for the fabrication of SF/CNF scaffolds having optimum mechanical reinforcement and electrical conductivity.

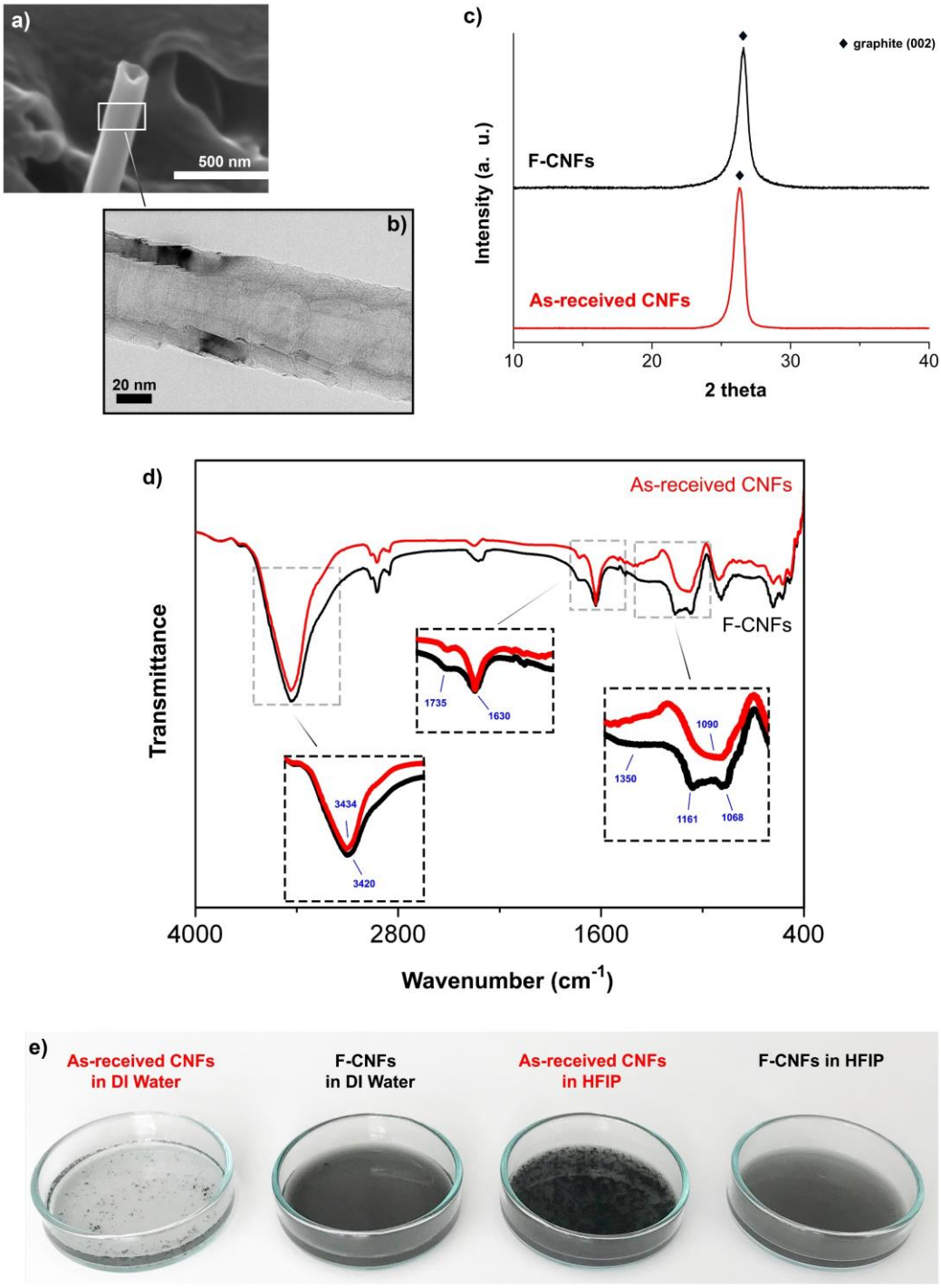

Figure 3.12. a) SEM, b) TEM image, c) XRD, d) FTIR spectra and e) dispersion of as-received CNFs and functionalized CNFs (F-CNFs).

In Figure 3.13, cross-sectional SEM images of SF-0C, SF-5C, SF-10C and SF-15C were given. SF-0C exhibited a relatively smooth appearance (Figure 3.13a), while randomly oriented CNFs were apparent on pore surfaces of SF-5C (Figure 3.13b). The fact that individual CNFs, rather than bundles, emerged from the cross-sectional surface of SF-5C and SF-10C (Figure 3.13c) indicated the well-dispersed nature of CNFs throughout these scaffolds. However, once CNF content increased to 15%, CNF bundling appeared on the cross-sectional images of the pore surfaces (Figure 3.13d). To gain more insight into the effect of CNF concentration on the nanophase surface roughness (Figure 3.13e, 3.13f and 3.13g), SF/CNF nanocomposite films having 0, 1, 3, 5 and 10% CNF were scanned using AFM. The AFM analysis revealed that nanophase surface roughness (rms) of nanocomposites having 0% CNF (2.4±0.5) was not significantly different than that of SF/CNF nanocomposites having 1, 3 and 5% CNF ($p>0.1$), such that their surface nanophase roughness values were measured to be 3±0.7, 3.9±1.5 and 3.6±0.4 nm, respectively. On the other hand, rms value of nanocomposite films increased up to 11.5±1.4 nm upon the incorporation of 10% CNF (Figure 3.13h). Comparing the AFM scans for SF films having 0 and 10% CNF, a smooth surface was observed for the former, while the embedded CNFs emerging from the SF provided a rougher surface topography for the latter. Thus, the increase in the surface nanophase roughness of SF with higher CNF concentration could be attributed to the bulging of CNFs from the SF matrix.

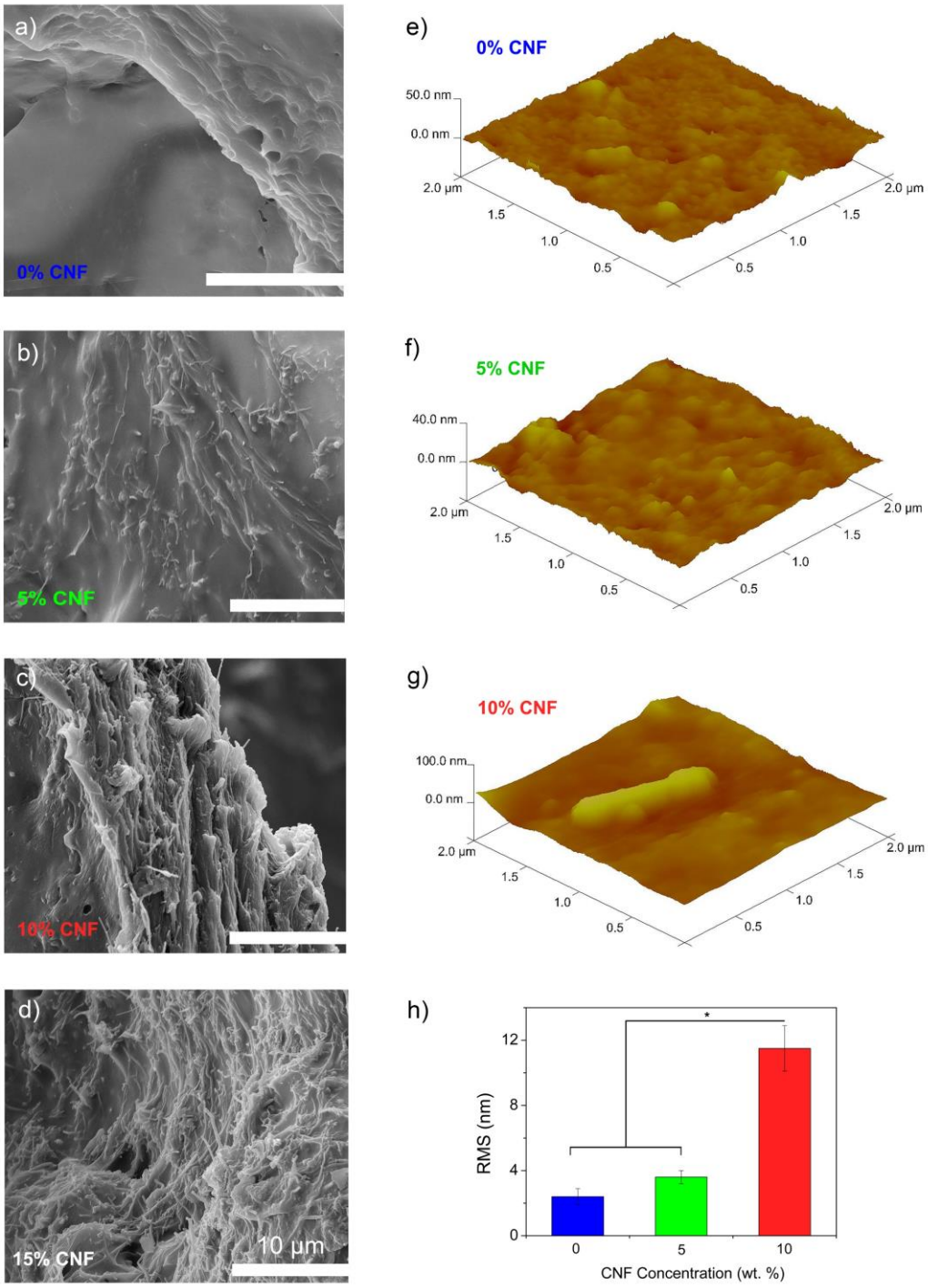

Figure 3.13. (a-d) Cross-sectional SEM images of SF scaffolds having a) 0, b) 5, c) 10 and d) 15% CNF, (e-g) AFM scans for SF having e) 0%, f) 5%, g) 10% CNF and h) RMS values of SF/CNF nanocomposites having 0, 1, 5 and 10 wt.% CNF. *p < 0.05.

FTIR spectra of SF-0C, SF-10C and L-SF were given in Figure 3.14a. In the FTIR spectra of SF-0C and SF-10C, peaks obtained at amide I and amide II regions shifted from ~1640 and ~1530 cm^{-1} (silk I) to ~1620 and ~1510 cm^{-1} indicating the formation of silk II structure. Also, an additional peak was obtained in the FTIR spectra of SF-0C and SF-10C at ~1265 cm^{-1} that further verified the formation of silk II structure. It was interesting to note that the intensities of peaks for SF-0C were higher compared to that of SF-10C. As a matter of fact, peak intensity and crystallinity decreased upon the addition of 10% CNF into SF matrix. It was also confirmed through deconvolution of amide I regions in the FTIR spectra of SF-0C and SF-10C. Results indicated that formation of β-sheets was hindered in the presence of CNFs. In fact, the β-sheet content of L-SF was increased from 23.2% to 39.1% for SF-0C, whereas it was increased up to 31.4% for SF-10C (Figure 3.14b and 3.14c, respectively).

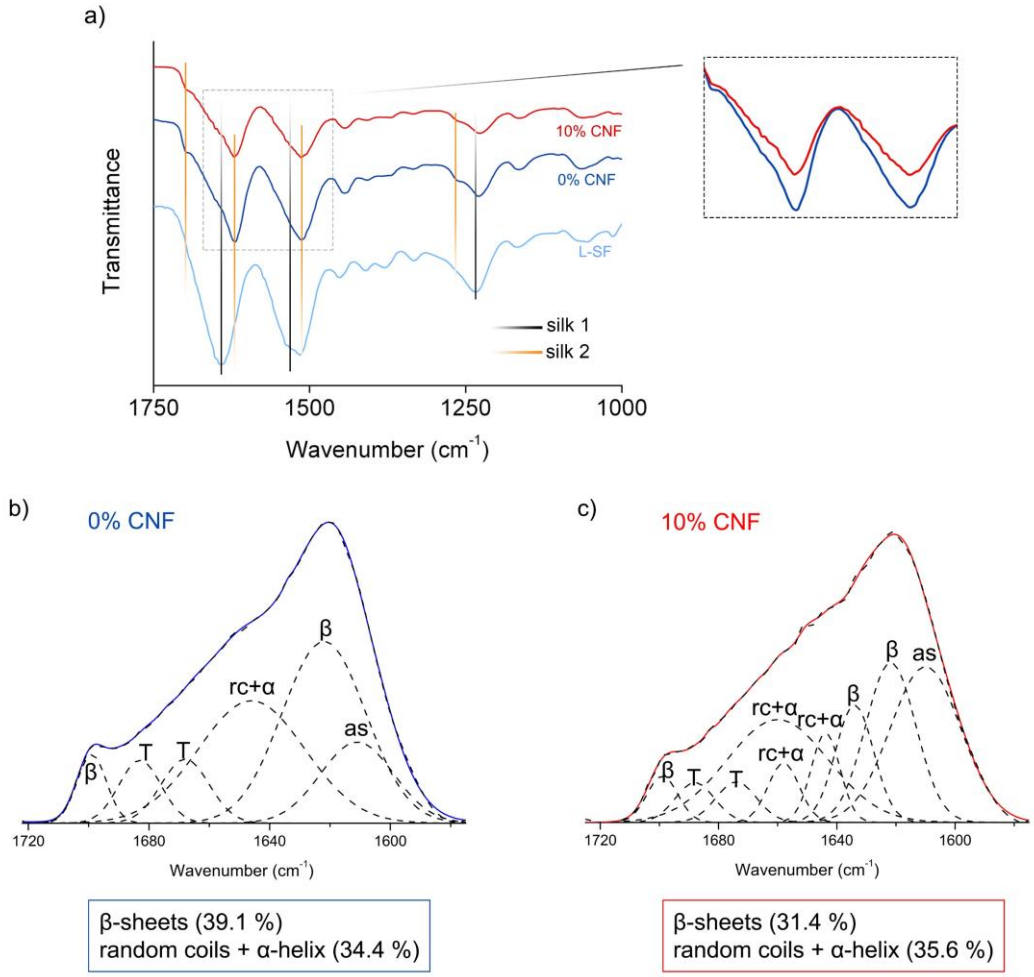

Figure 3.14. a) FTIR spectra of L-SF, 0% CNF and 10% CNF scaffolds, (b-c) fractions of secondary structural elements obtained from the amide I regions of b) 0% CNF and c) 10% CNF scaffolds. β: β-sheets, T: β-turns, rc+α: random coils + α-helix and as: aggregated strands.

This result was further confirmed with XRD analyses of SF-0C and SF-10C provided in the Figure 3.15 (XRD pattern of L-SF was also provided in the same figure). L-SF revealed the typical XRD pattern of amorphous SF [82]; however, β-sheet crystallite peaks at 20.4°, 21.1° and 23.4° were obtained for SF-0C [88][89][19]. On the other hand, SF-10C had two peaks at 21.2° and 23.6° corresponding to β-sheet crystallites and an additional peak at 26.3° corresponding to CNFs. The absence of β-sheet crystallite peak at 20.4° and the decreased intensities with slight shifts in the

peaks at 21.2° and 23.6° in the XRD pattern of SF-10C indicated decreased crystallinity upon the addition of 10% CNF.

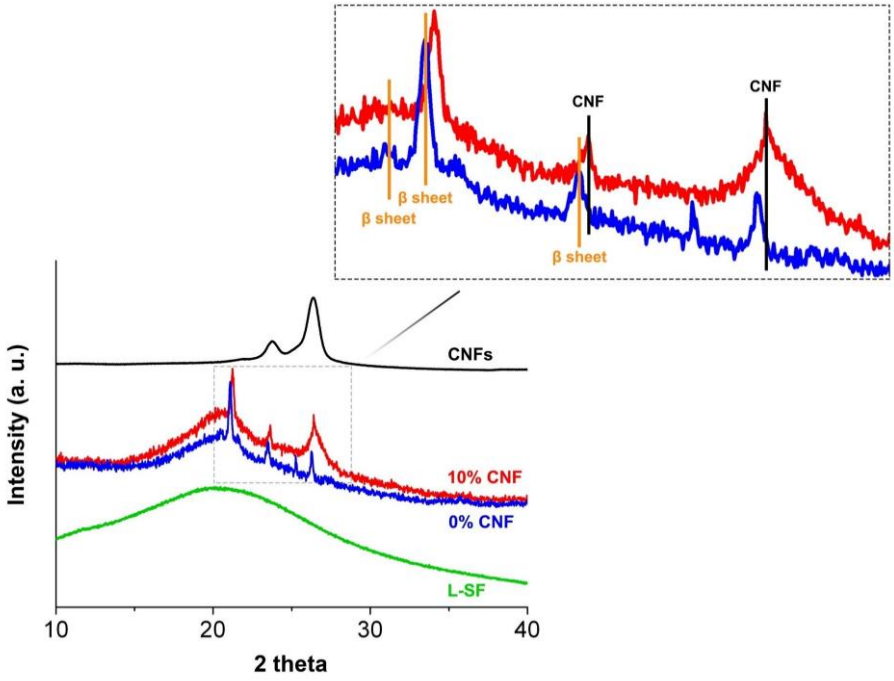

Figure 3.15. XRD spectra of CNFs, L-SF, SF-0C and SF-10C.

The stress-strain curves of SF-0C, SF-5C, SF-7.5C, SF-10C and SF-15C were plotted in Figure 3.16a. The tangent modulus of SF-0C was calculated to be 50±10 kPa and upon the incorporation of 5, 7.5 and 10% CNF, the modulus values increased up to 100±20, 150±40 and 260±30 kPa, respectively (Figure 3.16b). There was no further increase in the modulus with an additional incorporation of more CNFs into SF, i.e. SF-15C had a modulus of 250±50 kPa and it was not higher than that of SF-10C. Fractographic analysis of SF-10C and SF-15C showed dispersed CNFs with pull-out regions on SF-10C, as shown in Figure 3.16c where anchoring of CNFs within the SF matrix was evident. On the other hand, CNF bundles, rather than individual CNFs, were observed on the fracture surfaces of SF-15C (Figure 3.16d), which was in accord with the cross-sectional image shown in Figure 3.13d.

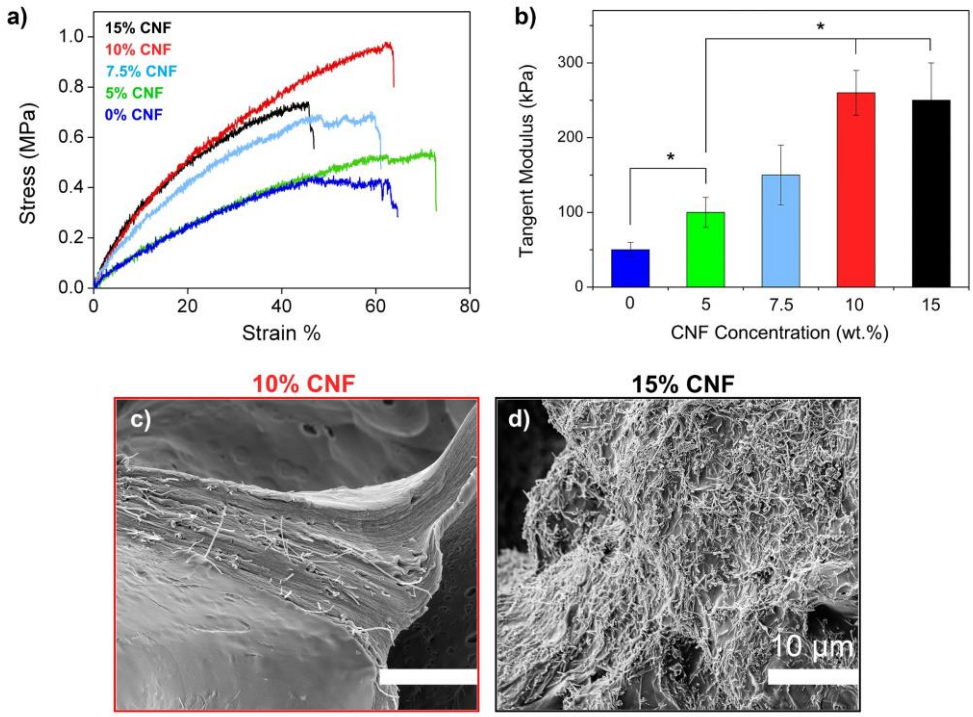

Figure 3.16. a) Stress-strain curves, b) tangent modulus values of SF/CNF nanocomposite scaffolds having 0, 5, 7.5, 10 and 15% CNFs, (c-d) fracture surfaces of scaffolds having c) 10% and d) 15% CNF. *$p < 0.05$.

Electrical conductivities of SF-0C, SF-5C, SF-7.5C, SF-10C and SF-15C were measured in dry state and the results were given in Figure 3.17. The conductivities of SF/CNF nanocomposite scaffolds (SF-0C, SF-1C and SF-3C) were undetectable up to 5% CNF with the analytical instruments used in this study. The electrical conductivity of SF-5C was measured to be ~0.002 S/cm and the conductivity measurements did not reveal a statistically significant difference between SF-5C and SF-7.5C. However, upon the incorporation of 10% CNF, electrical conductivity of the nanocomposite scaffolds increased up to ~0.04 S/cm. Interestingly, further increase in CNF concentration (SF-15C) ended up with a lower electrical conductivity of ~0.01 S/cm.

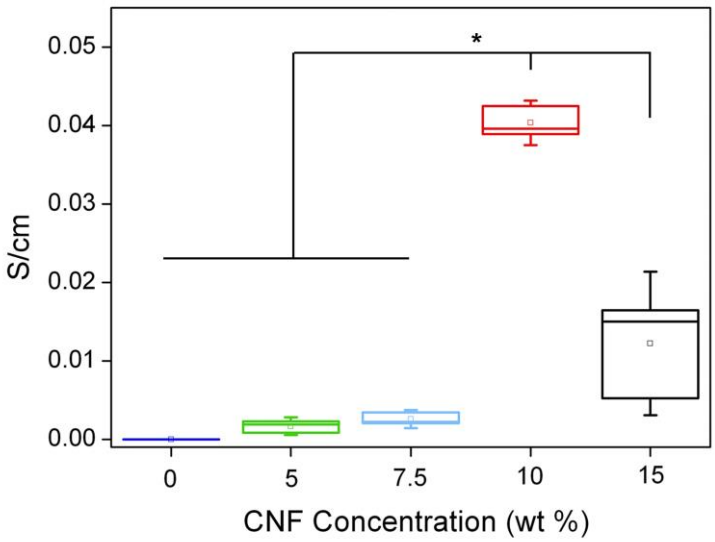

Figure 3.17. Electrical conductivities of SF scaffolds having up to 15 wt.% CNF. *p < 0.05.

Sessile drop water contact angles were measured to assess hydrophobicities of the SF/CNF nanocomposites and presented in Figure 3.18. A gradual decrease in the hydrophobicity was observed upon incorporation of CNFs into the SF matrix. Water contact angles of scaffolds were measured to be 97.9°±1.7°, 101.3°±0.5°, 82.2°±0.4°, 75.3°±1.1° and 64.0°±1.8° for SF-0C, SF-1C, SF-3C, SF-5C and SF-10C, respectively, indicating the hydrophilic nature of SF/CNF samples having 10% CNF.

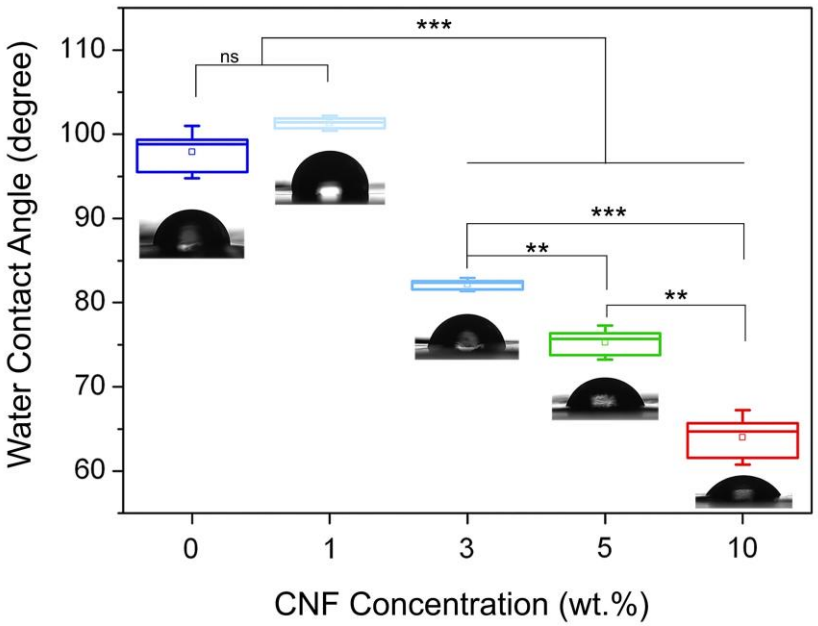

Figure 3.18. Water contact angles on SF/CNF nanocomposites having up to 10% CNFs. ** $p < 0.01$, *** $p < 0.001$.

Biological interactions of the porous SF/CNF scaffolds with L929 fibroblasts were given in Figure 3.19. Results revealed that all the tested scaffolds provided a suitable environment for cellular adhesion and proliferation up to 5 days *in vitro*. The adhesion of cells at 4hr of culture on SF-0C was higher than SF-10C, yet similar cellular densities were observed on SF-0C, SF-1C, SF-3C and SF-5C at 4hr *in vitro*. It is important to note that although cellular densities on 3, 5 and 10% CNF scaffolds were lower compared to 0% CNF scaffolds at 1, 3 and 5 days *in vitro*, cellular proliferation was observed -independent of the CNF concentration- on all scaffolds. Furthermore, fibroblasts cultured on SF-0C, Figure 3.19(b-c), and SF-10C, Figure 3.19(d-e), exhibited different cellular morphologies. The cells cultured on SF-10C spread more than the ones cultured on SF-0C. Cell surface coverage was 96.7±20.4 and 349.7±62.6 μm^2/cell for SF-0C and SF-10C, respectively (Figure 3.19f). Additionally, cells on SF-10C expressed more filopodia to interact with scaffold surfaces than the ones on SF-0C.

These findings were in-line with studies investigating the interactions of CNFs and CNF reinforced polymers with fibroblasts. For instance, Price et. al. [72] showed

that fibroblast adhesion was significantly less on polycarbonate urethane (PCU)/CNF nanocomposites compared to the pure PCU and it was decreased with increased amount of CNFs. However, they also showed enhanced adhesion of osteoblasts on PCU/CNF nanocomposites with increased amount of CNFs. It was suggested that the optimal surface energy varies for different cell types and the surface energy of the PCU/CNF nanocomposites might be too high for optimal fibroblast adhesion. In another study, interactions of SF/CNF nanocomposite films with fibroblasts were investigated [66]. Results showed that proliferation rates of cells were less on SF/CNF nanocomposite films having the highest CNF concentration. However, the proliferation rates of fibroblasts on SF/CNF nanocomposites having up to 5 wt.% CNFs were comparable with TCP. Furthermore, wettability of SF films was enhanced with increased CNF concentration which, in turn, resulted with broader cellular morphology on nanocomposites having up to 5 wt.% CNFs.

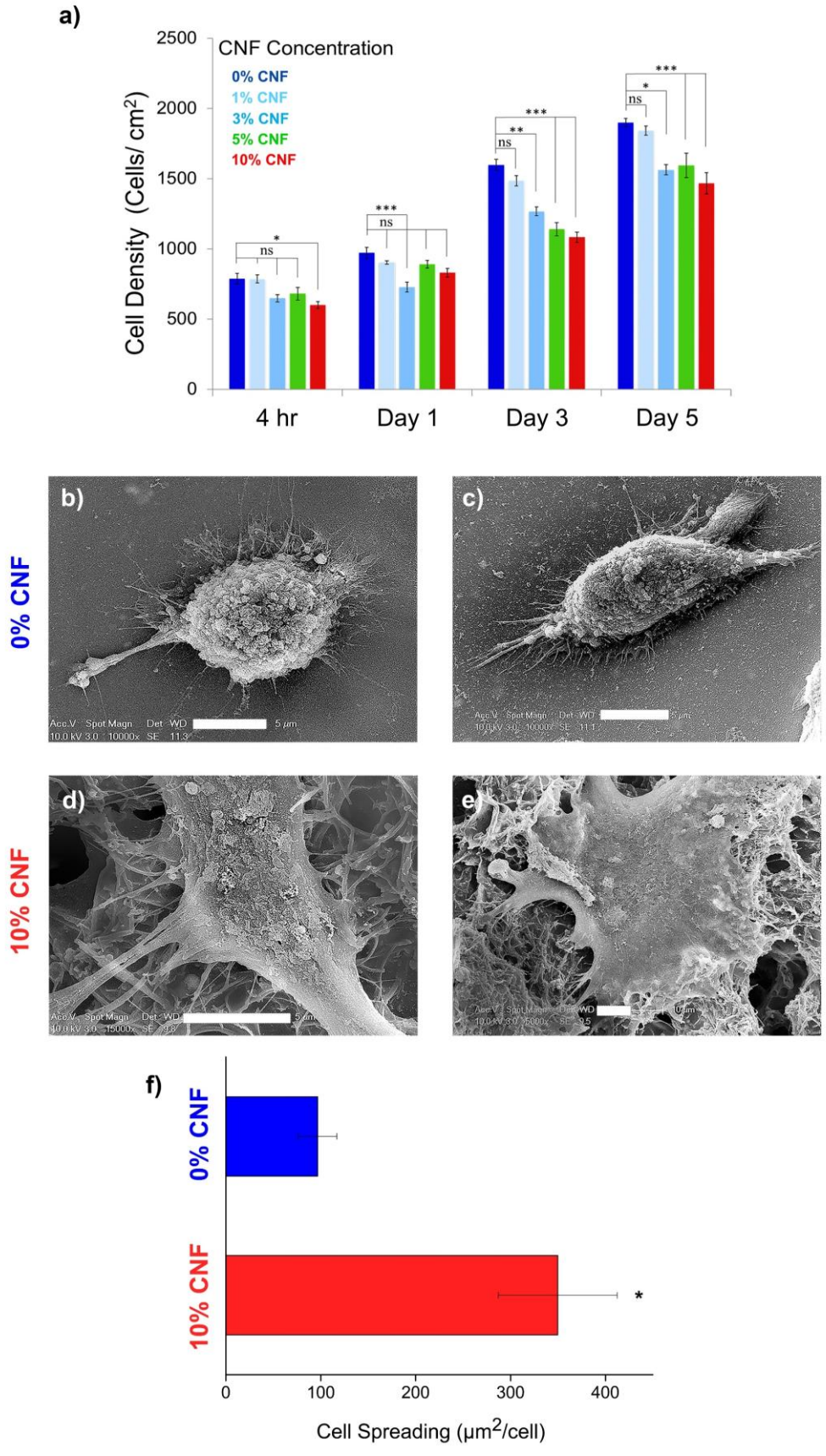
a)
CNF Concentration
0% CNF
1% CNF
3% CNF
5% CNF
10% CNF
Cell Density (Cells/ cm2)
2500
2000
1500
1000
500
0
4 hr
Day 1
Day 3
Day 5
ns
*
**
***
b)
c)
d)
e)
0% CNF
10% CNF
f)
0% CNF
10% CNF
0
100
200
300
400
Cell Spreading (μm2/cell)

Figure 3.19. a) Fibroblast densities on SF scaffolds prepared using various CNF concentrations. (b-c) and (d-e) SEM images of fibroblast cells on SF scaffolds having (b-c) 0 and (d-e) 10% CNFs (scale bars are 5 μm) and f) cell surface coverage values of fibroblast cells on SF scaffolds having 0 and 10 wt.% CNFs. *$p < 0.05$, ** $p < 0.01$, ***$p<0.001$, ****$p < 0.0001$.

CNFs are prone to form bundles due to their high surface energies. The nature of their interactions is via the Columbic forces and Van der Waals attractions [90]. However, CNFs should be dispersed homogeneously throughout the SF matrix to obtain optimum reinforcement in mechanical and electrical properties [91], which could only be achieved via overcoming the aforementioned secondary bonding between individual CNFs. Herein, we took advantage of the hydrogen bond forming ability of HFIP with the functional groups of CNFs (–COOH, -C=O and –OH) formed upon the acid treatment [92]. Our methodology consisted of dispersing CNFs in HFIP during the initial step of scaffold fabrication, followed by dissolving SF inside CNF dispersed HFIP. This approach inhibited the CNF bundling (even at 10% concentration) due to the formation of hydrogen bonds between HFIP molecules and CNFs (Fig. 3.20a), which could overcome Columbic forces and Van der Waals attractions between CNFs [92][93][94]. Another observation supporting this hypothesis was the dissolution rate of SF inside HFIP in the presence of CNFs. It was observed that the dissolution of SF in HFIP/CNF mixture was slower than that of CNF-free HFIP. It could be speculated that the already established molecular interactions between the functional groups on CNFs and HFIP molecules limited the interaction of amino acids in SF with HFIP, which, in turn, decreased the potential of HFIP to induce hydrogen bonding. This could further retard interaction of HFIP molecules with SF in the presence of CNFs and decrease SF dissolution rate inside HFIP [95]. Having this said, SF-0C and SF-10C scaffolds were immersed inside methanol for the same duration, yet more intense β-sheet peaks were detected for SF-0C compared to SF-10C. This was an indication of perturbed methanol interaction with the SF polypeptide in the presence of CNFs. It was possible to think that CNFs were physically inhibiting the interaction of methanol with SF, allowing

formation of weak chemical interactions between SF polypeptide chains and CNF functional groups, which, in turn, retarded protein folding and crystallization (Fig. 3.20b). Further research is required to understand the interactions between HFIP, SF and CNFs in the molecular level. However, our results clearly showed significant enhancements in the tangent modulus and electrical conductivities of porous SF/CNF nanocomposites, which suggested formation of a well-dispersed CNF secondary phase within porous SF matrix. It is important to note that, although the CNFs inhibited β-sheet formation (resulted in lower crystallinity), strengthening due to nanocomposite formation become decisive over tangent modulus of nanocomposites, *i.e.* overall effect of CNF incorporation was the significant enhancement of tangent modulus of scaffolds. Also, surfactants which could be detrimental to cellular functions [96], were not used to disperse the secondary CNF phase in our nanocomposite scaffold fabrication technique. The fracture surfaces also confirmed well-dispersed CNFs that were anchored to the SF matrix up to 10% CNF concentrations. Having this said, wettability and nanoscale surface roughness of SF, which were identified in literature to enhance cellular functions [97], were enhanced through the incorporation of 10% CNF. The increased hydrophilicity and nanophase roughness also led to better spreading of fibroblasts on SF-10C compared to SF-0C, while increased roughness provided a larger surface area for cellular interactions. It was also possible that the surface chemistry of SF scaffolds was altered at locations where CNFs protruded out of the SF matrices. This could also contribute to cell spreading, which enhanced more than 2.5 folds upon the addition of 10% CNF, owing to the hydroxyl groups on CNF surfaces [97]. The improved electrical conductivity, enhanced mechanical properties and better cellular spreading on SF-10C was promising for its utilization in tissue engineering applications. Specifically, the electrical conductivity and elastic modulus of the SF-10C scaffold match with those values observed for myocardium, suggesting the potential use of 3D SF/CNF nanocomposite scaffolds in cardiac patch applications.

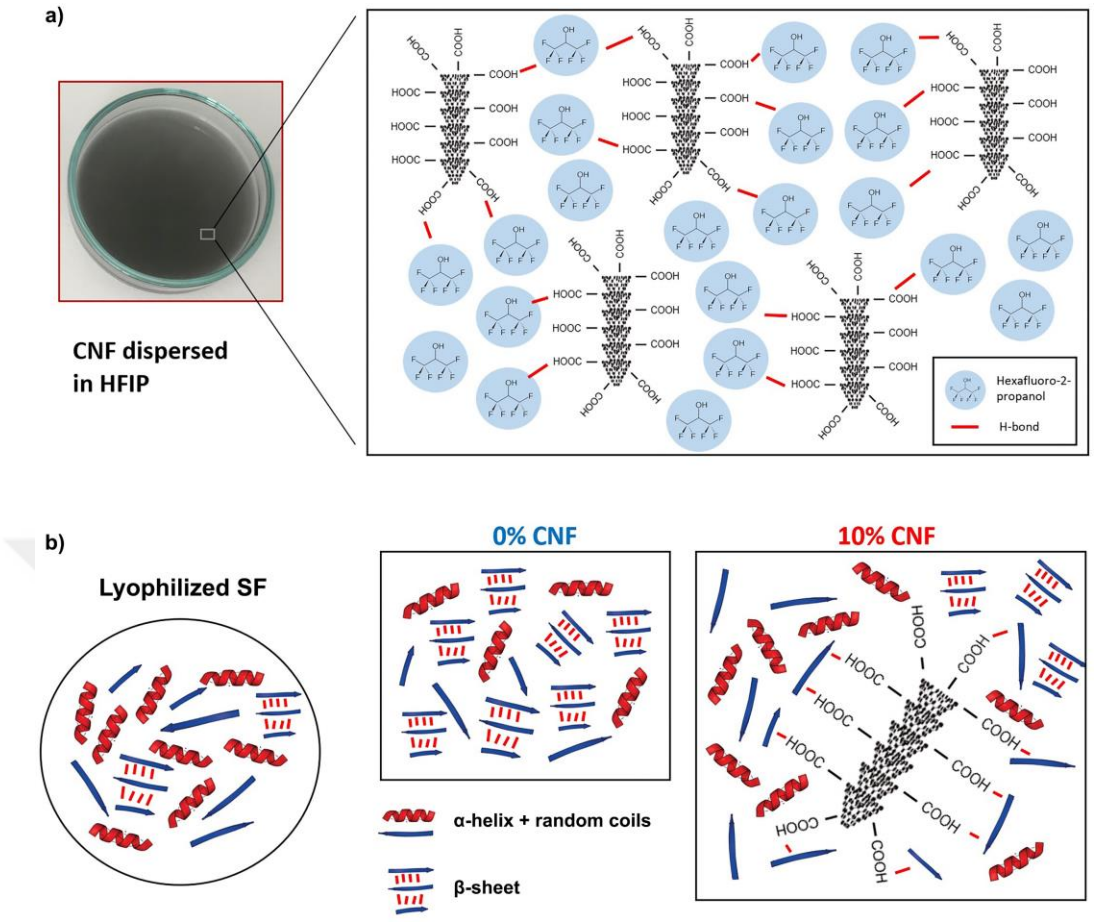

Figure 3.20. Schematic illustrations of a) possible dispersion mechanism of CNFs in HFIP and b) possible mechanism for the interactions of SF molecular chains with CNFs.

CHAPTER 4

CONCLUSIONS AND FUTURE WORK

To sum up, a porous architecture that provide enhanced cellular interactions together with desired mechanical properties was achieved through the optimization of SF scaffold fabrication parameters. Highly conductive nanocomposite scaffolds (up to ~0.04 S/cm) with enhanced tangent modulus (260±30 kPa) were fabricated owing to well-dispersed CNF secondary phase within the porous SF matrix. Furthermore, ~34% increase in the wettability of the nanocomposites was achieved upon the incorporation of 10% CNF, which provided enhanced fibroblast spreading on scaffold surfaces. These findings could potentially lead to development of 3D tissue scaffolds with enhanced mechanical and electrical properties.

Though this thesis showed the potential of porous SF/CNF nanocomposites to be used in tissue engineering applications, there are some additional points need to be investigated in the future. These points could be listed as following:

- Mechanical and electrical properties of SF/CNF nanocomposites were similar to that of cardiac tissue. Therefore, to investigate their potential use as cardiac patches, their interactions with cardiac muscle cells or cells that have the potential to differentiate into cardiac muscle cells, *i.e.* induced pluripotent stem cells (iPSC), needs to be addressed. For this purpose, cellular adhesion, proliferation and gene expressions (oct4, nanog, myl2 and ctnt) of iPSC need to be investigated.
- Considering SF/CNF nanocomposites to be used as cardiac patches, their mechanical properties under more realistic stress scenarios need to be investigated. Thus, biaxial tests need to be completed to better evaluate their mechanical integrity under stresses similar to the physiological environment.

- Degradation characteristics of SF/CNF nanocomposites needs to be characterized through proteolytic degradation tests (protease IV enzyme will be used). Time dependent changes in their mechanical and electrical properties needs to be investigated.
- Functionality of SF/CNF nanocomposites, *i.e.* the synchronized beating behaviour and the response to the electrical stimulation needs to be investigated.
- *In vivo* performance of SF/CNF nanocomposites needs to be assessed.

REFERENCES

[1] Khademhosseini A, Langer R. A decade of progress in tissue engineering. Nat Protoc 2016;11:1775–81. https://doi.org/10.1038/nprot.2016.123.

[2] Zhu W, Ma X, Gou M, Mei D, Zhang K, Chen S. 3D printing of functional biomaterials for tissue engineering. Curr Opin Biotechnol 2016;40:103–12. https://doi.org/10.1016/j.copbio.2016.03.014.

[3] Zhao P, Gu H, Mi H, Rao C, Fu J, Turng L sheng. Fabrication of scaffolds in tissue engineering: A review. Front Mech Eng 2018;13:107–19. https://doi.org/10.1007/s11465-018-0496-8.

[4] Dvir T, Timko BP, Kohane DS, Langer R. Nanotechnological strategies for engineering complex tissues. Nat Nanotechnol 2011;6:13–22. https://doi.org/10.1038/nnano.2010.246.

[5] Zhang X, Zhang Y. Tissue Engineering Applications of Three-Dimensional Bioprinting. Cell Biochem Biophys 2015;72:777–82. https://doi.org/10.1007/s12013-015-0531-x.

[6] Iqbal N, Khan AS, Asif A, Yar M, John W. Recent concepts in biodegradable polymers for tissue engineering paradigms : a critical review 2019;6608. https://doi.org/10.1080/09506608.2018.1460943.

[7] O'Brien FJ. Biomaterials & scaffolds for tissue engineering. Mater Today 2011;14:88–95. https://doi.org/10.1016/S1369-7021(11)70058-X.

[8] Nanomedicine R, Seifalian EA, Walmsley GG, Mcardle A, Tevlin R, Momeni A, et al. Nanotechnology in bone tissue engineering. Nanomedicine Nanotechnology, Biol Med 2015;11:1253–63. https://doi.org/10.1016/j.nano.2015.02.013.

[9] Belanger K, Dinis TM, Taourirt S, Vidal G, Kaplan DL, Egles C. Recent Strategies in Tissue Engineering for Guided Peripheral Nerve Regeneration

n.d.:472–81.

[10] Fomby P, Cherlin AJ, Hadjizadeh A, Doillon CJ, Sueblinvong V, Weiss DJ, et al. Stem cells and cell therapies in lung biology and diseases: Conference report. Ann Am Thorac Soc 2010;12:181–204. https://doi.org/10.1002/term.

[11] Badrossamay MR, McIlwee HA, Goss JA, Parker KK. Nanofiber assembly by rotary jet-spinning. Nano Lett 2010;10:2257–61. https://doi.org/10.1021/nl101355x.

[12] Sugiura T, Hibino N, Breuer CK, Shinoka T. Tissue-engineered cardiac patch seeded with human induced pluripotent stem cell derived cardiomyocytes promoted the regeneration of host cardiomyocytes in a rat model. J Cardiothorac Surg 2016;11:1–8. https://doi.org/10.1186/s13019-016-0559-z.

[13] Kitsara M, Agbulut O, Kontziampasis D, Chen Y, Menasché P. Fibers for hearts: A critical review on electrospinning for cardiac tissue engineering. Acta Biomater 2017;48:20–40. https://doi.org/10.1016/j.actbio.2016.11.014.

[14] Hayoun-Neeman D, Korover N, Etzion S, Ofir R, Lichtenstein RG, Cohen S. Exploring peptide-functionalized alginate scaffolds for engineering cardiac tissue from human embryonic stem cell-derived cardiomyocytes in serum-free medium. Polym Adv Technol 2019:1–13. https://doi.org/10.1002/pat.4602.

[15] Ho CMB, Mishra A, Lin PTP, Ng SH, Yeong WY, Kim YJ, et al. 3D Printed Polycaprolactone Carbon Nanotube Composite Scaffolds for Cardiac Tissue Engineering. Macromol Biosci 2017;17:1–9. https://doi.org/10.1002/mabi.201600250.

[16] Dvir T, Timko BP, Brigham MD, Naik SR, Karajanagi SS, Levy O, et al. Nanowired three-dimensional cardiac patches. Nat Nanotechnol 2011;6:720–5. https://doi.org/10.1038/nnano.2011.160.

[17] Rockwood DN, Preda RC, Wang X, Yucel T, Lovett ML. Materials Fabrication from Bombyx Mori Silk Fibroin. Natl Protoc 2013;6:1–43.

https://doi.org/10.1038/nprot.2011.379.Materials.

[18] Vepari C, Kaplan DL. Silk as Biomaterial. Prog Polym Sci 2007;100:130–4. https://doi.org/10.1016/j.pestbp.2011.02.012.Investigations.

[19] Peng Z, Yang X, Liu C, Dong Z, Wang F, Wang X, et al. Structural and Mechanical Properties of Silk from Different Instars of Bombyx mori. Biomacromolecules 2019;20:1203–16. https://doi.org/10.1021/acs.biomac.8b01576.

[20] Koh LD, Cheng Y, Teng CP, Khin YW, Loh XJ, Tee SY, et al. Structures, mechanical properties and applications of silk fibroin materials. Prog Polym Sci 2015;46:86–110. https://doi.org/10.1016/j.progpolymsci.2015.02.001.

[21] Du S, Zhang J, Zhou WT, Li QX, Greene GW, Zhu HJ, et al. Interactions between fibroin and sericin proteins from Antheraea pernyi and Bombyx mori silk fibers. J Colloid Interface Sci 2016;478:316–23. https://doi.org/10.1016/j.jcis.2016.06.030.

[22] Poza P, Pérez-Rigueiro J, Elices M, LLorca J. Fractographic analysis of silkworm and spider silk. Eng Fract Mech 2002;69:1035–48. https://doi.org/10.1016/S0013-7944(01)00120-5.

[23] Xu G, Gong L, Yang Z, Liu XY. What makes spider silk fibers so strong? from molecular-crystallite network to hierarchical network structures. Soft Matter 2014;10:2116–23. https://doi.org/10.1039/c3sm52845f.

[24] Wang Q, Ling S, Yao Q, Li Q, Hu D, Dai Q, et al. Observations of 3 nm Silk Nanofibrils Exfoliated from Natural Silkworm Silk Fibers. ACS Mater Lett 2020;2:153–60. https://doi.org/10.1021/acsmaterialslett.9b00461.

[25] Omenetto FG, Kaplan DL. New opportunities for an ancient material. Science (80-) 2010;329:528–31. https://doi.org/10.1126/science.1188936.

[26] Phillips DM, Drummy LF, Conrady DG, Fox DM, Naik RR, Stone MO, et al. Dissolution and Regeneration of Bombyx mori Silk Fibroin Using Ionic

Liquids 2004:14350–1. https://doi.org/10.1021/ja046079f.

[27] Janani G, Kumar M, Chouhan D, Moses JC, Gangrade A, Bhattacharjee S, et al. Insight into Silk-Based Biomaterials: From Physicochemical Attributes to Recent Biomedical Applications. ACS Appl Bio Mater 2019;2:5460–91. https://doi.org/10.1021/acsabm.9b00576.

[28] Joseph B, Raj SJ. Therapeutic applications and properties of silk proteins from Bombyx mori. Front Life Sci 2012;6:55–60. https://doi.org/10.1080/21553769.2012.760491.

[29] Pereira RFP, Silva MM, De Zea Bermudez V. Bombyx mori Silk Fibers: An Outstanding Family of Materials. Macromol Mater Eng 2015;300:1171–98. https://doi.org/10.1002/mame.201400276.

[30] Qiu W, Patil A, Hu F, Liu XY. Hierarchical Structure of Silk Materials Versus Mechanical Performance and Mesoscopic Engineering Principles. Small 2019;15:1–45. https://doi.org/10.1002/smll.201903948.

[31] Taura JRS. Jin and Kaplan - Mechanism of silk processing in insects and spiders 2003;926:1057–61.

[32] Cebe P, Partlow BP, Kaplan DL, Wurm A, Zhuravlev E, Schick C. Silk I and Silk II studied by fast scanning calorimetry. Acta Biomater 2017;55:323–32. https://doi.org/10.1016/j.actbio.2017.04.001.

[33] Compound Interest. A Brief Guide to the Twenty Common Amino Acids – Compound Interest 2016. https://www.compoundchem.com/2014/09/16/aminoacids/ (accessed July 3, 2020).

[34] Keten S, Xu Z, Ihle B, Buehler MJ. Nanoconfinement controls stiffness, strength and mechanical toughness of B-sheet crystals in silk. Nat Mater 2010;9:359–67. https://doi.org/10.1038/nmat2704.

[35] Ribeiro VP, da Silva Morais A, Maia FR, Canadas RF, Costa JB, Oliveira AL,

et al. Combinatory approach for developing silk fibroin scaffolds for cartilage regeneration. Acta Biomater 2018;72:167–81. doi.org/10.1016/j.actbio.2018.03.047.

[36] Xie M, Song L, Wang J, Fan S, Zhang Y, Xu Y. Evaluation of stretched electrospun silk fibroin matrices seeded with urothelial cells for urethra reconstruction. J Surg Res 2013;184:774–81. https://doi.org/10.1016/j.jss.2013.04.016.

[37] Kim DK, Sim BR, Kim JI, Khang G. Functionalized silk fibroin film scaffold using β-Carotene for cornea endothelial cell regeneration. Colloids Surfaces B Biointerfaces 2018;164:340–6. https://doi.org/10.1016/j.colsurfb.2017.11.052.

[38] Bhattacharjee P, Kundu B, Naskar D, Kim HW, Maiti TK, Bhattacharya D, et al. Silk scaffolds in bone tissue engineering: An overview. Acta Biomater 2017;63:1–17. https://doi.org/10.1016/j.actbio.2017.09.027.

[39] Chouhan D, Lohe T u., Samudrala PK, Mandal BB. In Situ Forming Injectable Silk Fibroin Hydrogel Promotes Skin Regeneration in Full Thickness Burn Wounds. Adv Healthc Mater 2018;7:1–15. https://doi.org/10.1002/adhm.201801092.

[40] Yang MC, Wang SS, Chou NK, Chi NH, Huang YY, Chang YL, et al. The cardiomyogenic differentiation of rat mesenchymal stem cells on silk fibroin-polysaccharide cardiac patches in vitro. Biomaterials 2009;30:3757–65. https://doi.org/10.1016/j.biomaterials.2009.03.057.

[41] Stoppel WL, Hu D, Domian IJ, Kaplan DL, Black LD. Anisotropic silk biomaterials containing cardiac extracellular matrix for cardiac tissue engineering. Biomed Mater 2015;10. https://doi.org/10.1088/1748-6041/10/3/034105.

[42] Patra C, Talukdar S, Novoyatleva T, Velagala SR, Mühlfeld C, Kundu B, et al. Silk protein fibroin from Antheraea mylitta for cardiac tissue engineering.

Biomaterials 2012;33:2673–80. https://doi.org/10.1016/j.biomaterials.2011.12.036.

[43] Loh QL, Choong C, Oxon D, Hons M, Mimmm C. Three-Dimensional Scaffolds for Tissue Engineering Applications : 2013;19. https://doi.org/10.1089/ten.teb.2012.0437.

[44] Yan LP, Oliveira JM, Oliveira AL, Caridade SG, Mano JF, Reis RL. Macro/microporous silk fibroin scaffolds with potential for articular cartilage and meniscus tissue engineering applications. Acta Biomater 2012;8:289–301. https://doi.org/10.1016/j.actbio.2011.09.037.

[45] Correia C, Bhumiratana S, Yan LP, Oliveira AL, Gimble JM, Rockwood D, et al. Development of silk-based scaffolds for tissue engineering of bone from human adipose-derived stem cells. Acta Biomater 2012;8:2483–92. https://doi.org/10.1016/j.actbio.2012.03.019.

[46] Thimm BW, Wüst S, Hofmann S, Hagenmüller H, Müller R. Initial cell pre-cultivation can maximize ECM mineralization by human mesenchymal stem cells on silk fibroin scaffolds. Acta Biomater 2011;7:2218–28. https://doi.org/10.1016/j.actbio.2011.02.004.

[47] Wang Y, Bella E, Lee CSD, Migliaresi C, Pelcastre L, Schwartz Z, et al. The synergistic effects of 3-D porous silk fibroin matrix scaffold properties and hydrodynamic environment in cartilage tissue regeneration. Biomaterials 2010;31:4672–81. https://doi.org/10.1016/j.biomaterials.2010.02.006.

[48] Vishwanath V, Pramanik K, Biswas A. Optimization and evaluation of silk fibroin-chitosan freeze-dried porous scaffolds for cartilage tissue engineering application. J Biomater Sci Polym Ed 2016;27:657–74. https://doi.org/10.1080/09205063.2016.1148303.

[49] Eng JT, Med R, Mueller D, Tascher G, Ursula M, Knobeloch D, et al. In-depth physiological characterization of primary human hepatocytes in a 3D hollow-fiber bioreactor. J Tissue Eng Regen Med 2011:51–64.

https://doi.org/10.1002/term.

[50] Mandal BB, Kundu SC. Cell proliferation and migration in silk fibroin 3D scaffolds. Biomaterials 2009;30:2956–65. https://doi.org/10.1016/j.biomaterials.2009.02.006.

[51] Mandal BB, Kundu SC. Non-mulberry silk gland fibroin protein 3-D scaffold for enhanced differentiation of human mesenchymal stem cells into osteocytes. Acta Biomater 2009;5:2579–90. https://doi.org/10.1016/j.actbio.2009.02.033.

[52] Rnjak-Kovacina J, Wray LS, Burke KA, Torregrosa T, Golinski JM, Huang W, et al. Lyophilized Silk Sponges: A Versatile Biomaterial Platform for Soft Tissue Engineering. ACS Biomater Sci Eng 2015;1:260–70. https://doi.org/10.1021/ab500149p.

[53] Zhang Q, Zhao Y, Yan S, Yang Y, Zhao H, Li M, et al. Preparation of uniaxial multichannel silk fibroin scaffolds for guiding primary neurons. Acta Biomater 2012;8:2628–38. https://doi.org/10.1016/j.actbio.2012.03.033.

[54] Bose S, Roy M, Bandyopadhyay A. Recent advances in bone tissue engineering scaffolds. Trends Biotechnol 2012;30:546–54. https://doi.org/10.1016/j.tibtech.2012.07.005.

[55] McKee CT, Last JA, Russell P, Murphy CJ. Indentation versus tensile measurements of young's modulus for soft biological tissues. Tissue Eng - Part B Rev 2011;17:155–64. https://doi.org/10.1089/ten.teb.2010.0520.

[56] Stout DA, Yoo J, Santiago-Miranda AN, Webster TJ. Mechanisms of greater cardiomyocyte functions on conductive nanoengineered composites for cardiovascular applications. Int J Nanomedicine 2012;7:5653–69. https://doi.org/10.2147/IJN.S34574.

[57] Nge TT, Nogi M, Yano H, Sugiyama J. Microstructure and mechanical properties of bacterial cellulose/chitosan porous scaffold. Cellulose

2010;17:349–63. https://doi.org/10.1007/s10570-009-9394-x.

[58] Kim UJ, Park J, Joo Kim H, Wada M, Kaplan DL. Three-dimensional aqueous-derived biomaterial scaffolds from silk fibroin. Biomaterials 2005;26:2775–85. https://doi.org/10.1016/j.biomaterials.2004.07.044.

[59] Engler AJ, Sen S, Sweeney HL, Discher DE. Matrix Elasticity Directs Stem Cell Lineage Specification 2006:677–89. https://doi.org/10.1016/j.cell.2006.06.044.

[60] Wingate K, Bonani W, Tan Y, Bryant SJ, Tan W. Acta Biomaterialia Compressive elasticity of three-dimensional nanofiber matrix directs mesenchymal stem cell differentiation to vascular cells with endothelial or smooth muscle cell markers. Acta Biomater 2012;8:1440–9. https://doi.org/10.1016/j.actbio.2011.12.032.

[61] Gupta P, Sharan S, Roy P, Lahiri D. Aligned carbon nanotube reinforced polymeric scaffolds with electrical cues for neural tissue regeneration. Carbon N Y 2015;95:715–24. https://doi.org/10.1016/j.carbon.2015.08.107.

[62] Wang L, Wu Y, Hu T, Guo B, Ma PX. Electrospun conductive nanofibrous scaffolds for engineering cardiac tissue and 3D bioactuators. Acta Biomater 2017;59:68–81. https://doi.org/10.1016/j.actbio.2017.06.036.

[63] Burnstine-Townley A, Eshel Y, Amdursky N. Conductive Scaffolds for Cardiac and Neuronal Tissue Engineering: Governing Factors and Mechanisms. Adv Funct Mater 2019;1901369:1901369. https://doi.org/10.1002/adfm.201901369.

[64] Dozois MD, Bahlmann LC, Zilberman Y, Tang X (Shirley). Carbon nanomaterial-enhanced scaffolds for the creation of cardiac tissue constructs: A new frontier in cardiac tissue engineering. Carbon N Y 2017;120:338–49. https://doi.org/10.1016/j.carbon.2017.05.050.

[65] Gupta P, Agrawal A, Murali K, Varshney R, Beniwal S, Manhas S, et al.

Differential neural cell adhesion and neurite outgrowth on carbon nanotube and graphene reinforced polymeric scaffolds. Mater Sci Eng C 2019;97:539–51. https://doi.org/10.1016/j.msec.2018.12.065.

[66] Naskar D, Bhattacharjee P, Ghosh AK, Mandal M, Kundu SC. Carbon Nanofiber Reinforced Nonmulberry Silk Protein Fibroin Nanobiocomposite for Tissue Engineering Applications. ACS Appl Mater Interfaces 2017;9:19356–70. https://doi.org/10.1021/acsami.6b04777.

[67] Tran PA, Zhang L, Webster TJ. Carbon nanofibers and carbon nanotubes in regenerative medicine. Adv Drug Deliv Rev 2009;61:1097–114. https://doi.org/10.1016/j.addr.2009.07.010.

[68] Tran PA, Zhang L, Webster TJ. Carbon nanofibers and carbon nanotubes in regenerative medicine. Adv Drug Deliv Rev 2009;61:1097–114. https://doi.org/10.1016/j.addr.2009.07.010.

[69] Al-Saleh MH, Sundararaj U. A review of vapor grown carbon nanofiber/polymer conductive composites. Carbon N Y 2009;47:2–22. https://doi.org/10.1016/j.carbon.2008.09.039.

[70] Liu H, Cai Q, Lian P, Fang Z, Duan S, Ryu S, et al. The biological properties of carbon nanofibers decorated with β-tricalcium phosphate nanoparticles. Carbon N Y 2010;48:2266–72. https://doi.org/10.1016/j.carbon.2010.02.042.

[71] Elias KL, Price RL, Webster TJ. Enhanced functions of osteoblasts on nanometer diameter carbon fibers. Biomaterials 2002;23:3279–87. https://doi.org/10.1016/S0142-9612(02)00087-X.

[72] Price RL, Waid MC, Haberstroh KM, Webster TJ. Selective bone cell adhesion on formulations containing carbon nanofibers. Biomaterials 2003;24:1877–87. https://doi.org/10.1016/S0142-9612(02)00609-9.

[73] Martins AM, Eng G, Caridade SG, Mano JF, Reis RL, Vunjak-Novakovic G. Electrically conductive chitosan/carbon scaffolds for cardiac tissue

engineering. Biomacromolecules 2014;15:635–43. https://doi.org/10.1021/bm401679q.

[74] Chen MC, Sun YC, Chen YH. Electrically conductive nanofibers with highly oriented structures and their potential application in skeletal muscle tissue engineering. Acta Biomater 2013;9:5562–72. https://doi.org/10.1016/j.actbio.2012.10.024.

[75] Webster TJ, Waid MC, McKenzie JL, Price RL, Ejiofor JU. Nano-biotechnology: Carbon nanofibres as improved neural and orthopaedic implants. Nanotechnology 2004;15:48–54. https://doi.org/10.1088/0957-4484/15/1/009.

[76] Stout DA, Basu B, Webster TJ. Poly(lactic-co-glycolic acid): Carbon nanofiber composites for myocardial tissue engineering applications. Acta Biomater 2011;7:3101–12. https://doi.org/10.1016/j.actbio.2011.04.028.

[77] Naskar D, Ghosh AK, Mandal M, Das P, Nandi SK, Kundu SC. Dual growth factor loaded nonmulberry silk fibroin/carbon nanofiber composite 3D scaffolds for in vitro and in vivo bone regeneration. Biomaterials 2017;136:67–85. https://doi.org/10.1016/j.biomaterials.2017.05.014.

[78] Endo M, Kim YA, Hayashi T, Fukai Y, Oshida K, Terrones M, et al. Structural characterization of cup-stacked-type nanofibers with an entirely hollow core. Appl Phys Lett 2002;80:1267–9. doi.org/10.1063/1.1450264.

[79] Lammel AS, Hu X, Park SH, Kaplan DL, Scheibel TR. Controlling silk fibroin particle features for drug delivery. Biomaterials 2010;31:4583–91. https://doi.org/10.1016/j.biomaterials.2010.02.024.

[80] Hu X, Kaplan D, Cebe P. Determining beta-sheet crystallinity in fibrous proteins by thermal analysis and infrared spectroscopy. Macromolecules 2006;39:6161–70. https://doi.org/10.1021/ma0610109.

[81] Nazarov, Rina; Jin, Hyoung-Joon; kaplan DL. Porous 3-D Scaffolds from

Regenerated Silk Fibroin. Biomacromolecules 2004;5:718–26.

[82] Wang HY, Zhang YQ. Effect of regeneration of liquid silk fibroin on its structure and characterization. Soft Matter 2013;9:138–45. https://doi.org/10.1039/c2sm26945g.

[83] Zhou JH, Sui ZJ, Li P, Chen D, Dai YC, Yuan WK. Structural characterization of carbon nanofibers formed from different carbon-containing gases. Carbon N Y 2006;44:3255–62. https://doi.org/10.1016/j.carbon.2006.06.028.

[84] Zhou JH, Sui ZJ, Zhu J, Li P, Chen D, Dai YC, et al. Characterization of surface oxygen complexes on carbon nanofibers by TPD, XPS and FT-IR. Carbon N Y 2007;45:785–96. https://doi.org/10.1016/j.carbon.2006.11.019.

[85] Moraes FC, Cabral MF, Mascaro LH, MacHado SAS. The electrochemical effect of acid functionalisation of carbon nanotubes to be used in sensors development. Surf Sci 2011;605:435–40. https://doi.org/10.1016/j.susc.2010.11.014.

[86] Stobinski L, Lesiak B, Kövér L, Tóth J, Biniak S, Trykowski G, et al. Multiwall carbon nanotubes purification and oxidation by nitric acid studied by the FTIR and electron spectroscopy methods. J Alloys Compd 2010;501:77–84. https://doi.org/10.1016/j.jallcom.2010.04.032.

[87] Saleh TA. The influence of treatment temperature on the acidity of MWCNT oxidized by HNO 3 or a mixture of HNO 3 /H 2 SO 4. Appl Surf Sci 2011;257:7746–51. https://doi.org/10.1016/j.apsusc.2011.04.020.

[88] Lu Q, Hu X, Wang X, Kluge JA, Lu S, Cebe P, et al. Water-insoluble silk films with silk I structure. Acta Biomater 2010;6:1380–7. doi.org/10.1016/j.actbio.2009.10.041.

[89] Um IC, Kweon HY, Park YH, Hudson S. Structural characteristics and properties of the regenerated silk fibroin prepared from formic acid. Int J Biol Macromol 2001;29:91–7. doi.org/10.1016/S0141-8130(01)00159-3.

[90] Kabir ME, Saha MC, Jeelani S. Effect of ultrasound sonication in carbon nanofibers/polyurethane foam composite. Mater Sci Eng A 2007;459:111–6. doi.org/10.1016/j.msea.2007.01.031.

[91] Prolongo SG, Burón M, Gude MR, Chaos-Morán R, Campo M, Ureña A. Effects of dispersion techniques of carbon nanofibers on the thermo-physical properties of epoxy nanocomposites. Compos Sci Technol 2008;68:2722–30. https://doi.org/10.1016/j.compscitech.2008.05.015.

[92] Colomer I, Chamberlain AER, Haughey MB, Donohoe TJ. Hexafluoroisopropanol as a highly versatile solvent. Nat Rev Chem 2017;1. https://doi.org/10.1038/s41570-017-0088.

[93] Said Z, Allagui A, Abdelkareem MA, Alawadhi H, Elsaid K. Acid-functionalized carbon nanofibers for high stability, thermoelectrical and electrochemical properties of nanofluids. J Colloid Interface Sci 2018;520:50–7. https://doi.org/10.1016/j.jcis.2018.02.042.

[94] Aravind SSJ, Baskar P, Baby TT, Sabareesh RK, Das S, Ramaprabhu S. Investigation of structural stability, dispersion, viscosity, and conductive heat transfer properties of functionalized carbon nanotube based nanofluids. J Phys Chem C 2011;115:16737–44. doi.org/10.1021/jp201672p.

[95] Sashina ES, Bochek AM, Novoselov NP, Kirichenko DA. Structure and solubility of natural silk fibroin. Russ J Appl Chem 2006;79:869–76. https://doi.org/10.1134/S1070427206060012.

[96] Dong L, Joseph KL, Witkowski CM, Craig MM. Cytotoxicity of single-walled carbon nanotubes suspended in various surfactants. Nanotechnology 2008;19. https://doi.org/10.1088/0957-4484/19/25/255702.

[97] Chang H-I, Wang Y. Cell Responses to Surface and Architecture of Tissue Engineering Scaffolds. Regen. Med. Tissue Eng. - Cells Biomater., 2011. doi.org/10.5772/21983.